Multiscale investigation of cement pastes with low and high-grade calcined clays and slag at early and advanced ages

Imane Bekrine, Benoit Hilloulin, Ahmed Loukili

Multiscale investigation of cement pastes with low and high-grade calcined clays and slag at early and advanced ages

I. Bekrine[1], B. Hilloulin[1], A. Loukili[1]

Nantes Université, Ecole Centrale Nantes, CNRS, Institut de Recherche en Génie Civil et Mécanique (GeM), UMR 6183, F-44000 Nantes, France

ABSTRACT

Clays are abundant materials worldwide, but the massive demand for pure kaolinitic clays in multiple fields could reduce the availability of high-grade calcined clay. For this reason, the properties of cementitious materials with low-grade calcined clays should be seriously investigated. In this work, binary and ternary binders composed of high-grade or low-grade calcined clays and slag, replacing 30% of Portland cement, are studied using nanoindentation, standard strength measurement, MIP, and SEM in order to demonstrate the impact of calcined clay composition on the microscale and macroscale properties of cementitious materials during both early and mature ages. Results show that in binary binders, low-grade calcined clay leads to reduced porosity and enhanced elastic and viscoelastic properties, as probed by means of nanoindentation, while high-grade calcined clay results in a high amount of low-density calcium silicate hydrate (LD CSH). Moreover, in the ternary binder, a synergistic effect has been highlighted between low-grade calcined clay and slag through the improvement of compressive strength at early age, as well as a refinement of the pore structure. From this study, it can be concluded that low-grade calcined clays give rise to good micromechanical properties and can be particularly effective in ternary blends when associated with slag.

Keywords: Nanoindentation, Micromechanical Properties, Creep, Microstructure, Calcined Clay, Blast Furnace Slag.

Summary of abbreviations

Mineral additions

SCMs	Supplementary cementitious materials
CC	Calcined clay
GBFS	Granulated blast furnace slag

Pastes' phases

LD CSH	Low-density CSH
HD CSH	High-density CSH
CH	Portlandite/calcium hydroxide
UC	Unhydrated cement
Q	Quartz
M	Muscovite

Atomic species

Al	Aluminium
K	Potassium
Ca	Calcium
Si	Silicon

Experimental and numerical techniques

XRD	X-ray diffraction
SEM	Scanning electron microscope
EDS	Energy dispersive spectroscopy
BSE	Backscattered electrons
MIP	Mercury intrusion porosity
TGA	Thermogravimetric analysis
GMM	Gaussian Mixture Model

1. Introduction

Cement production is a highly CO_2-emitting process. Its main constituent, clinker, is obtained by limestone and natural clays being fired at 1,450°C, which requires fossil fuels for heating and induces limestone decarbonation. To reduce this substantial environmental impact, supplementary cementitious materials (SCMs) can partially replace cement in concrete. Commonly used SCMs include fly ash, silica fume and granulated blast furnace slag; however, these are only available in limited supplies. Fine limestone and natural pozzolans are also employed, but their reactivity remains low when used alone. The introduction of calcined clays in cement blends has thus received great

attention of late due to their smaller carbon footprint, widespread availability [1] and potential to improve cementitious material properties.

Replacing a portion of Portland cement with calcined clays results in several changes in the cement paste hydration products. In addition to calcium-silicate-hydrate (CSH), calcium hydroxide (CH) and ettringite, which are the main hydration products of a Portland cement paste, other products may be formed depending on the raw clay composition. For instance, the alumina-rich amorphous phase of metakaolin (MK) triggers the formation of calcium aluminosilicate hydrates (CASH), CAH, strätlingite C_2ASH_8, and hydrogranet C_3AH_6 or C_4AH_{13}, depending on both the AS_2/CH ratio (AS_2 stands for Al_2O_3 . $2SiO_2$) and reaction temperature [2]. In the presence of reactive calcite, calcium hemicarboaluminate hydrates (Hc) are also formed as a consequence of ettringite conversion [3]. The hydration kinetics are also modified with calcined clay incorporation, since they accelerate the hydration of clinker minerals, with ettringite being formed faster [4], which also increases the heat of hydration, as reported in [5]. Moreover, calcined clays are pozzolanic materials, which results in calcium hydroxide consumption inside the cement paste after several days/weeks [6].

Overall, it has been proven that incorporating calcined clays is beneficial to cementitious materials, as regards the majority of their properties. It has also been shown that compressive strength increases relative to pure cement reference samples, especially at early ages, given that the filler effect is immediate [7], as is the elastic modulus [8,9]. Durability properties may actually be enhanced with calcined clay incorporation through pore size refinement [10]. In their study, Dwivedi *et al.* pointed out that a 20% replacement of cement by metakaolin in mortars reduces the number of capillary pores, thus leading to decreased permeability [11]. Chloride ion ingress is also reduced [12,13], as is the resistance to freeze-thaw cycles [14].

However, the use of calcined clays in cementitious systems also has some drawbacks, such as a loss of workability due to its high specific surface area [15]. The use of other SCMs with calcined clays can serve to overcome these obstacles and enhance other properties. Recently, several studies have demonstrated the efficiency of using calcined clays with limestone in LC^3 binders, in improving chloride resistance [16,17] and preventing the alkali-silica reaction [18]. Similarly, the use of calcined clays with slag improves fluidity of the cement blend [19] as well as compressive strength [20]. Even though several works have studied the hydration and macromechanical properties of calcined clay-based cementitious blends, their micromechanical properties are rarely addressed, especially at an early age. In addition, the effect of the calcined clay grade on several properties of cementitious materials was studied, such as rheology [21], hydration and mechanical performance [22–24],

printability [25], but there is no such study to determine its effect on micromechanical properties, namely elastic modulus, hardness, and contact creep modulus, of the cementitious materials phases, which is of huge importance to understand the observed behaviors at the macroscale.

Microindentation and nanoindentation were applied as local mechanical investigation techniques in order to assess the mechanical properties of cementitious materials [26]. Some studies used these techniques to investigate localized phenomena, such as the interfacial transition zone (ITZ) [27,28] and carbonated areas [29], while others targeted specific phases of interest in a heterogeneous material [30]. Nonetheless, since cementitious materials exhibit heterogeneous features, the majority of studies performed a large number of indentations in the regular grid forms so as to study the cement pastes; the properties of the various phases were determined by means of different clustering methods, namely least-square estimation (LSE) and maximum likelihood estimation (MLE) [31–33]. A number of studies on pure cement mixes were conducted according to these techniques [34–36], then extending to mixes containing SCMs to assess their effect on micromechanical properties. The elastic modulus of the CSH phase was indeed found to be 10% lower when silica fume and fly ash were incorporated [37], while another study demonstrated that the elastic properties did not change with fly ash incorporation [38]. Instead, the fractions of portlandite decreased and those of high-density CSH increased [37,38], which was explained by the pozzolanic reaction. Evidence of the pozzolanic reaction has also been proven in the presence of metakaolin [39] and slag [40]. The incorporation of pure metakaolin (96.4% amorphous phase) and slag resulted in an increase of CSH porosity at 7 days [41].

Over the last two decades, a study of the viscoelastic behavior of materials subjected to microindentation and nanoindentation techniques has been added as well. These techniques have speeded the characterization of creep properties of cementitious materials by applying a constant load for several tens of seconds on the tested materials; in contrast, measuring creep properties typically takes weeks to years at the scale of concrete laboratory samples or actual structures [42,43]. Although the creep mechanism of cementitious materials has yet to be well understood, it is generally agreed that CSH acts as the primary cause. In [44,45], the authors proved that CSH exhibits logarithmic creep properties that depend solely on CSH packing density. Several studies were subsequently conducted to investigate the creep properties of cementitious materials [43-45]. Li and colleagues have examined the effect of various cement paste phases on cement paste creep properties and underscored the importance of considering the actual pore creep modulus instead of 0 GPa, as well as the possibility of considering all unhydrated particles, despite a wide range of creep property variation, as a single phase in homogenization schemes [49]. The impact of SCMs on viscoelastic

properties has rarely been assessed although they may play a significant role in the modern green concrete creep phenomenon. Li *et al.* have shown that a 10% cement replacement with silica fume was found to enhance the CSH creep modulus [50]; but to the best of the authors' knowledge, no such studies on calcined clay binary or ternary blends have yet to be conducted, especially at an early age.

In this study, the micromechanical properties of binary and ternary calcined clay-blended pastes at both early and advanced ages will be investigated, and the advantage of using low-grade calcined clays in terms of performance will be demonstrated, along with their availability, lower environmental impact (due to lower calcination temperatures) and lower cost. To this end, a comprehensive comparison of the pastes microstructure and nanoindentation-inferred micromechanical properties will be drawn between low-grade and high-grade calcined clay-based cement pastes. Next, the effect of slag addition on the Portland cement / low-grade calcined clay system will be discussed and the synergistic effect of slag and low-grade calcined clay highlighted.

2. Materials and methods

2.1 Materials and sample preparation

The materials used in this study are Portland cement CEM I 52.5 N, two distinct calcined clays CC1 and CC2, respectively originated from "Charentes" and "Mariais" extraction sites in France, and granulated blast furnace slag (GBFS). The chemical composition and physical properties of the binders are given in

Table 1.

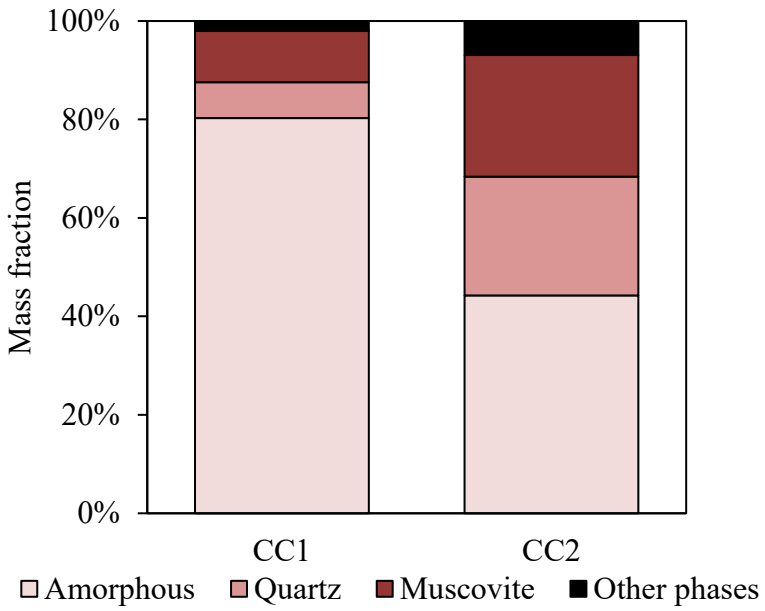

Fig. 1 shows the mineralogical composition of the studied calcined clays obtained by means of XRD and quantified by Rietveld analysis using the external standard method. According to the figure, CC1 and CC2 are mostly composed of amorphous phase (80.2% and 44.2% resp.), muscovite (10.4% and 24.7% resp.) and quartz (7.3% and 24.1% resp.). Other phases were identified in minor amounts such as kaolinite, rutile, albite and mullite. In the rest of this paper, CC1 and CC2 will be respectively assigned as high-grade and low-grade calcined clays given their amorphous phase content. The impact of this difference in calcined clays composition on the micromechanical properties of cement pastes will be investigated.

Table 1

Chemical and physical properties of the materials used in this study

		Cement	**GBFS**	**CC1**	**CC2**
Chemical composition (%)	SiO_2	20.4	37.7	53.95	62.70
	Al_2O_3	4.4	10.2	38.48	27.86
	Fe_2O_3	2.3	0.6	1.82	2.98
	TiO_2	-	0.7	1.53	0.35
	CaO	64.0	43.8	0.04	0.10
	MgO	3.9	6.4	0.19	0.39
	SO_3	2.9	0.1	-	-
	K_2O	0.66	0.28	1.04	2.50
	Na_2O	0.15	0.21	0.10	0.14
	P_2O_5	0.1	-	0.07	0.08
	Cl^-	0.02	0.02	-	-
	S^{2-}	<0.02	0.7	-	-
	Na_2O eq.	0.58	0.44	-	-
Physical properties	Specific gravity (g/cm^3)	3.15	2.9	2.2	2.5
	Specific area (cm^2/g)	3979	4450	190000	160000

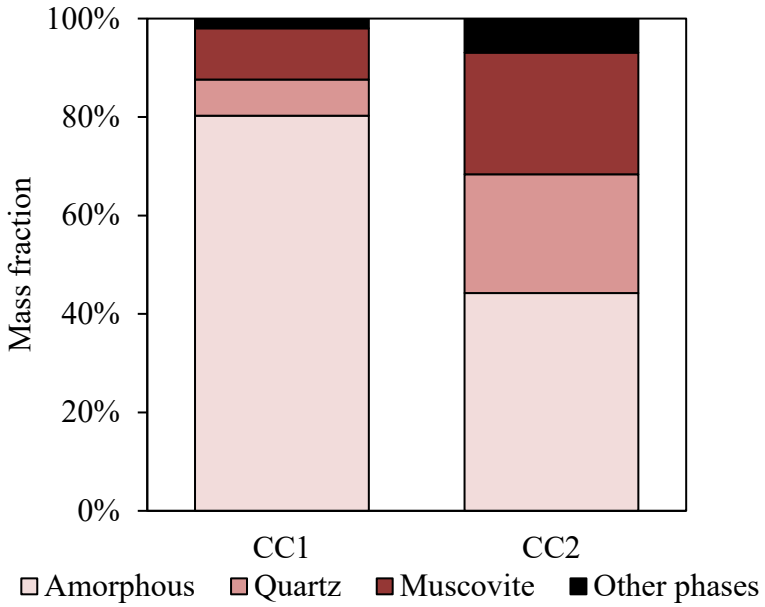

142

143 **Fig. 1.** Calcined clay compositions as determined using XRD/Rietveld analysis

144 Using these raw materials, water and superplasticizer (depending on the mix workability), four
145 cement pastes with a constant water-to-binder ratio of 0.3 were manufactured. 30% of cement (by
146 volume) was replaced by mineral additions in the binary and ternary binders. The binder proportions
147 are detailed in Table 2.

148 **Table 2**

149 Cement paste binder compositions (volume proportions)

Paste reference	Cement (%)	GBFS (%)	CC1 (%)	CC2 (%)
P_0	100	-	-	-
$PCC1_{30}$	70	-	30	-
$PCC2_{30}$	70	-	-	30
$PCC2_{15}S_{15}$	70	15	-	15

150

151 The 4 × 4 × 16 cm^3 cement paste prisms were manufactured, standard cured, demolded at 24 h and
152 kept in lime-saturated water at 20°C until reaching testing age. Then, 1-2 cm cubes were sawn at the
153 testing age, placed in 99.8% isopropanol for 4 days to stop hydration, and dried at 40°C for 4 other
154 days [51]. As explained in [52], all hydration stoppage procedures were proven to cause microscopic
155 modifications to the sample, although isopropanol is weaker and causes less damage.

156 For the nanoindentation and SEM tests, the cubes were impregnated in cold mounting epoxy resin.
157 Special care was paid to the sample polishing step in order to achieve smooth surfaces: coarse

158 polishing was performed using SiC abrasive papers of decreasing grain sizes from 120 to 4000 grit
159 (corresponding resp. to 68 µm - 5.3 µm), then fine polishing using diamond pastes on woven natural
160 silk discs of 3 µm and 1 µm grain sizes. Ethanol was used as a polishing lubricant to prevent further
161 hydration. After each polishing step, the samples were cleaned in an ethanol ultrasonic bath for a few
162 minutes to remove all suspensions and debris on the surface. Surface quality was assessed by means
163 of the Scanning Probe Microscopy (SPM) mode of the nanoindenter, with the Root Mean Square
164 (RMS) roughness being calculated on 50 × 50 µm² surfaces.

165 *2.2 Methods*

166 2.2.1 Macromechanical testing

167 The compressive strength was measured on 4 × 4 × 16 cm^3 prisms previously split into two, on at
168 least four samples at 2 and 28 days according to NF EN 196-1 standard.

169 2.2.2 Thermogravimetric analysis

170 Portlandite content in the mixes was determined using TGA in order to assess the binders' pozzolanic
171 activity, according to ASTM C1872-18 standard. For this purpose, a NETZSCH microbalance was
172 used with N_2 purging gas and a rate of 60 mL/min. 50 ± 5 mg of crushed powder were placed in
173 alumina crucibles and subjected to raising temperatures from 20°C to 1000°C with a heating rate of
174 10°C/min. The weight loss WL_{CH} (%) of portlandite due to the evaporation of water was determined
175 using the tangential method of Marsh [53] between 400°C and 550°C, and the measured mass
176 proportion mm_{CH}(%) of portlandite as well as its actual mass proportion in the sample m_{CH}(%) are
177 deduced using respectively the equations below:

178 $$mm_{CH}(\%) = WL_{CH} \times \frac{M_{CH}}{M_{H_2O}} \quad (1)$$

179 $$m_{CH}(\%) = \frac{mm_{CH}(\%)}{m_{600°C} \times \left(1 + \frac{w}{b}\right)} \quad (2)$$

180 where M_{CH}=74 g/mol is the molar mass of portlandite, M_{H_2O}=18 g/mol is the molar mass of water,
181 $m_{600°C}$ is the sample mass at 600°C and w/b=0.3 is the water-to-binder ratio of all cement pastes.

182 2.2.3 Mercury intrusion porosity

183 The pore structure of the various cement pastes was investigated using a Micromeritics AutoPore IV
184 mercury porosimeter according to ISO 15901-1:2016 standard. The mercury pressure gauge was used
185 at a maximum pressure of 400 MPa, which corresponds to a minimum pore radius of 1.5 nm. Each
186 cement paste mix was tested at 2 and 28 days.

2.2.4 Scanning electron microscopy - Energy dispersive spectroscopy (SEM/EDS)

Scanning electron microscopy equipped with X-ray energy dispersive spectroscopy (SEM/EDS) was conducted to characterize the blended cement pastes microstructures. Backscattered electron (BSE) images were captured using an accelerating voltage of 15 kV, at working distance of 17 mm and a magnification of 300×. A surface scan of the chemical composition with an EDS detector was needed to roughly detect the nature of certain observed phases on BSE micrographs through the resulting elemental maps.

2.2.5 Nanoindentation

Nanoindentation experiments were performed using a Bruker TS 77 Berkovich nanoindenter, in order to study the micromechanical properties of individual phases of the cement pastes. While in SPM mode, the smoothest parts of the samples (RMS < 50 nm) were targeted in order to carry out nanoindentation tests. Three grids of 20 × 20 indents, equally spaced at 5 µm, were executed using a load-controlled function, with a trapezoidal loading composed of a loading phase in 5 s, a holding phase of 60 s at maximum load P_{max} of 2 mN and an unloading phase of 5 s. Continuous measurements of penetration depth with these applied loads were recorded at a frequency of 200 Hz; consequently, the slope of the unloading curve at maximum load S could be determined.

The reduced elastic modulus E_r, elastic modulus E and hardness H were all then calculated as per the Oliver and Pharr method [54]:

$$E_r = \frac{1}{2}\sqrt{\frac{\pi}{A_c}}S \tag{3}$$

$$\frac{1}{E_r} = \frac{1-\nu^2}{E} + \frac{1-\nu_{ind}^2}{E_{ind}} \tag{4}$$

$$H = \frac{P_{max}}{A_c} \tag{5}$$

where ν is the material Poisson's ratio, which equals 0.24 for cement paste [55]; $\nu_{ind} = 0.07$ and $E_{ind} = 1{,}141$ GPa are respectively the diamond indenter Poisson's ratio and its elastic modulus. A_c denotes the projected contact area between the indenter tip and the indented surface, as obtained by the tip-area function calibration on a fused silica standard sample with incremental loads ranging from 100 µN to 10,000 µN by 100 µN increments.

In order to calculate viscoelastic properties from the nanoindentation tests, the variation in penetration depth $\Delta h(t) = h(t) - h_0$, where h_0 represents the initial penetration depth, is logarithmically fitted as:

$$\Delta h(t) = x_1 \, ln(1 + x_2 t) \tag{6}$$

where x_1 and x_2 are the parameters to fit; they are related to the creep modulus and characteristic time respectively by the following expressions:

$$C = \frac{P_{max}}{2 a_U x_1} \tag{7}$$

$$\tau = \frac{1}{x_2} \tag{8}$$

where $a_U = \sqrt{A_c/\pi}$ is the contact radius.

All abnormal load-depth curves [56] were deleted prior to conducting a statistical analysis of the results.

2.2.6 Deconvolution process

The analysis of each indentation curve provides information about the mechanical properties of each point k in the grid, i.e. values of elastic modulus, hardness and contact creep modulus (E_k, H_k, C_k). In this deconvolution process, the total distribution x of both elastic modulus and hardness $x = (E, H)$ was assumed a mixture of individual phases, where each phase is seen as a two-dimensional Gaussian distribution. The statistical deconvolution is then performed to cluster all the data into N mixture components, i.e. N clusters. The number of clusters was chosen based on the Bayesian Information Criterion (BIC). The probability density function of the Gaussian Mixture Model (GMM) is given in equation (9), and the one for each phase is given in equation (11):

$$p(x) = \sum_{i=1}^{N} \pi_i \, N(x|\mu_i, \Sigma_i) \tag{9}$$

$$\sum_{i=1}^{N} \pi_i = 1 \tag{10}$$

$$N(x|\mu, \Sigma) = \frac{1}{\sqrt{\det(2\pi\Sigma)}} e^{-\frac{1}{2}(x-\mu)\Sigma^{-1}(x-\mu)} \tag{11}$$

where π_i, μ_i and $\Sigma_i$are respectively the weighting coefficient, the mean value and the covariance of the i-th component.

To find the parameters (the weighting coefficient, the mean and the covariance) that maximize the joint probability, the following optimization problem is solved using Monte-Carlo search:

$$\max(\ln(\prod_{j=1}^{M} p(x_j))) = \max(\sum_{j=1}^{M} ln\left(\sum_{i=1}^{N} \pi_i N(x|\mu_i, \Sigma_i)\right) \quad (12)$$

where M is the number of observations, which is the number of indents.

To achieve this, Expectation-Maximization (EM) algorithm was used, where data were assigned to the closest randomly chosen means, the means recalculated based on the assigned data and so on until the calculated means are no more changing. Initial values were given by K-means algorithm in order to reduce the calculation time. This first step of calculation was referred to as (1) in Fig. 2 illustrating the calculation process. Finally, the mean and standard deviation of contact creep modulus on the CSH resulting clusters were calculated for all the samples, which was referred to as (2) in Fig. 2.

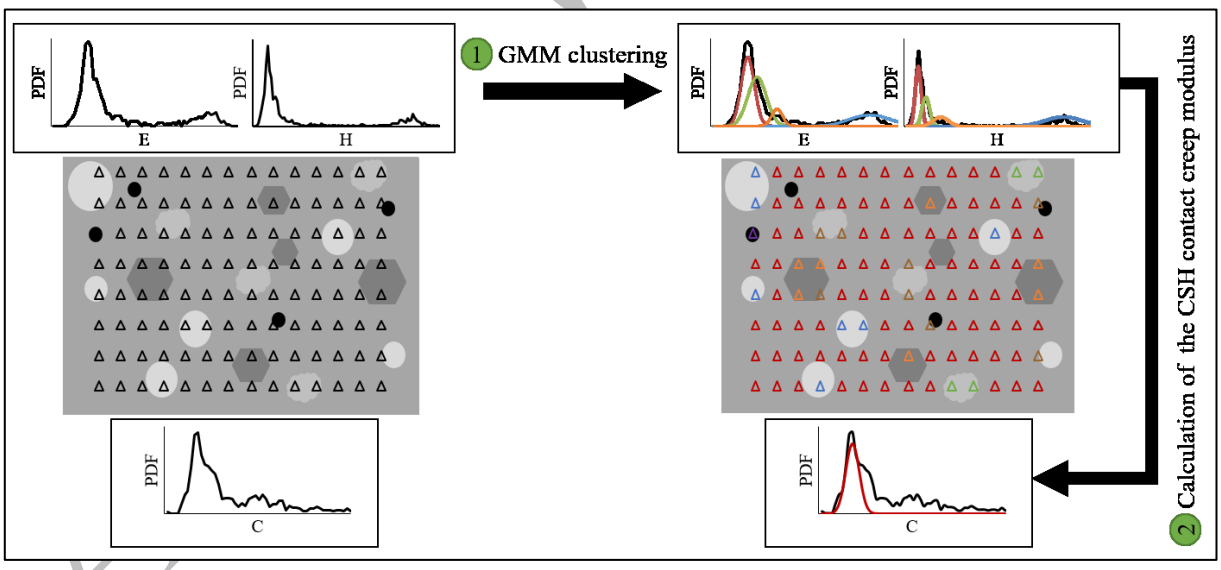

Fig. 2. Calculation process of the clusters micromechanical properties

The clusters determined by this deconvolution process do not necessarily correspond to pure phases, but the predominant ones can be determined depending on the mean and standard deviation values of E and H. In literature, the properties of the known main phases in Portland cement pastes (LD and HD CSH, portlandite, unhydrated cement) were widely reported. In addition to these known phases,

the values of elastic properties of some others, contained in our pastes and brought by the mineral additions, are given in Table 3 with the references from the literature. The assignment of predominant phases in each cluster starts by looking at the standard deviation: if it is high with respect to the mean value, then the cluster contains more than a predominant phase; if it is low, then the cluster is mono-phase. Then, the cluster's mean property is compared to values reported in the literature to assign suitable phase(s) to each cluster.

Table 3

Elastic properties of some phases in the literature (mean or mean ± standard deviation)

Phase	E (GPa)	H (GPa)	Reference
Unhydrated slag	72.4 ± 8.7	5.06 ± 1.18	[40]
Quartz	77.4	10.2	[57]
Muscovite	55.6	2.7	[57]

3. Results

3.1 Macroscopic compressive strength

Fig. 3 compares the compressive strength of the four cementitious systems at 2 and 28 days. First, we can notice a strength-gain from 2 to 28 days in all the mixes, which is higher for the blended cement pastes compared to the reference mix, and the highest in $PCC2_{30}$ with 57.7% gain. At 2 days, the average compressive strength of the reference mix and $PCC1_{30}$ are maximum, reaching nearly 60 MPa. Incorporating CC2 into the system causes a drop in compressive strength of 25.7% relative to the reference mix. This finding indicates a better mechanical performance for $PCC1_{30}$ at an early age. Incorporating slag with CC2 increased by 17.2% the compressive strength with respect to $PCC2_{30}$, which suggests a synergistic effect between the two additions. At 28 days, $PCC1_{30}$ developed the highest compressive strength among all cement blends. Interestingly, $PCC2_{30}$ developed an equivalent compressive strength to the reference mix, therefore proving the benefit of using low-grade calcined clay. It is also worth noting that small differences in strength were obtained between the ternary binder and the reference mix.

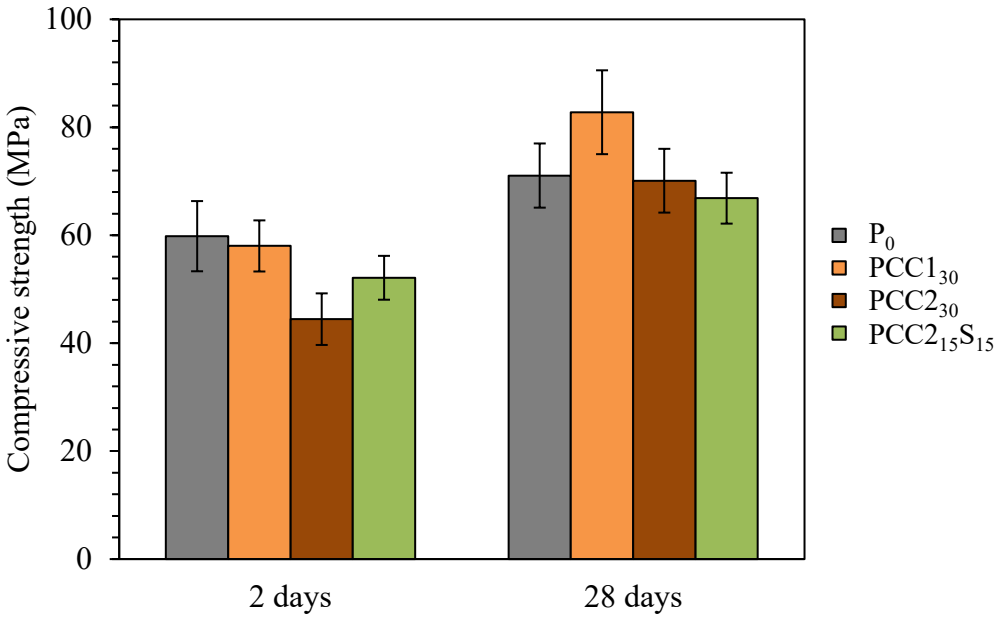

277

278 **Fig. 3.** Compressive strength of the cement paste mix designs at 2 and 28 days

279

280 *3.2 Microstructure investigation*

281 3.2.1 Pozzolanic activity

282 Portlandite content was accurately quantified by means of thermogravimetric analysis as shown in
283 Fig. 4. First of all, it can be noticed that the P_0 mixture showed the highest portlandite content at early
284 and mature ages, whereas it was lower in $PCC1_{30}$, $PCC2_{30}$ and $PCC2_{15}S_{15}$ due to clinker dilution
285 effect and secondary hydration reactions. When comparing both binary binders, $PCC1_{30}$ had a lower
286 portlandite content which suggests that CC1 has a higher pozzolanic potential than CC2 leading to
287 more portlandite consumption. The low portlandite content for $PCC1_{30}$ at 2 days suggests that
288 portlandite started being consumed at least at this point of hydration and thus that CC1 did already
289 start reacting. The portlandite content continues to decrease until 28 days of hydration with CC1 use.
290 Portlandite content do not seem to decrease in $PCC2_{30}$ at 28 days, which can be a result of the filler
291 effect of CC2 high quartz content, promoting further portlandite formation and compensating its
292 consumption by pozzolanic reactivity. The ternary binder shows lower pozzolanicty compared to
293 binary binders, suggesting the hydration of slag and more portlandite formation especially at 28 days.

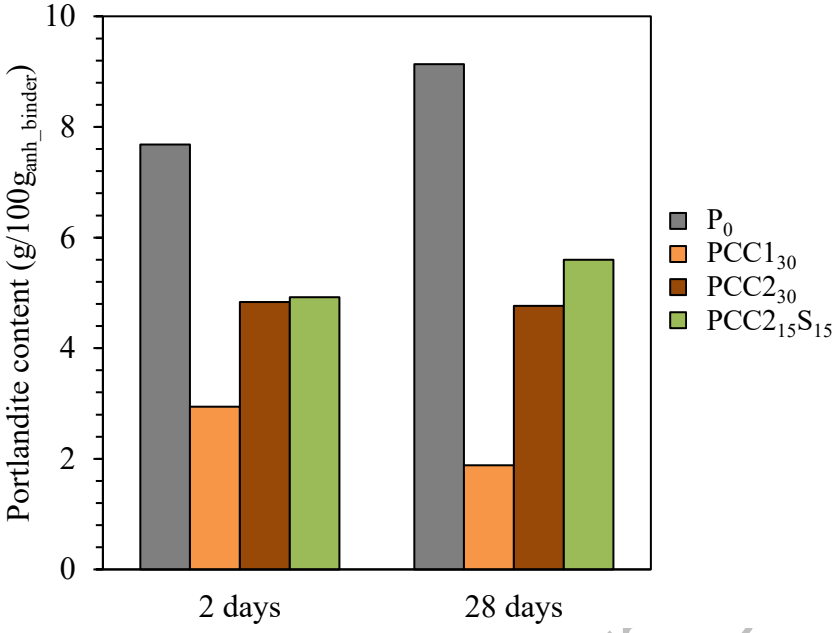

294

295 **Fig. 4.** Portlandite content (per g of anhydrous binder) of the cement paste mix designs at 2 and 28
296 days as determined by TGA

297

298 3.2.2 Pore structure

299 Fig. 5 displays the pore diameter distribution of each cement paste at both 2 and 28 days. It can be
300 noticed that total porosity decreases from 2 to 28 days across all mixes, which is to be expected as
301 hydration fills the pores. In addition, the pore structure changes significantly from 2 to 28 days in the
302 cement blends, given the domination of pores with a diameter smaller than 0.01 µm at 28 days, as
303 opposed to a diameter of between 0.01 and 0.1 µm at 2 days. This result was reported in [58] for
304 metakaolin-incorporated pastes, and was explained by its pozzolanic reaction that results in higher
305 amounts of CSH phase.

306 It can also be noticed that the total porosity of binary blends is higher than that of the reference mix,
307 especially at early age. However, the quantity of pores with a diameter of between 0.01 and 0.1 µm
308 is considerably reduced in the binary mixes, especially at 28 days. Moreover, the similar pore
309 structure of these binders is refined, potentially enhancing durability properties. It is interesting to
310 note that the low-grade calcined clay blend is less porous than $PCC1_{30}$, especially at early age, most
311 likely due to the presence of quartz, which has a crystalline phase of minor porosity. As for the ternary
312 blend, it can be noticed that the amount of total porosity is comparable to that of the reference mix at
313 2 and 28 days, yet the quantity of capillary pores is significantly reduced, especially at 28 days in the
314 ternary binder, which could lead to enhanced durability properties, proving a good synergy between
315 GBFS and CC2.

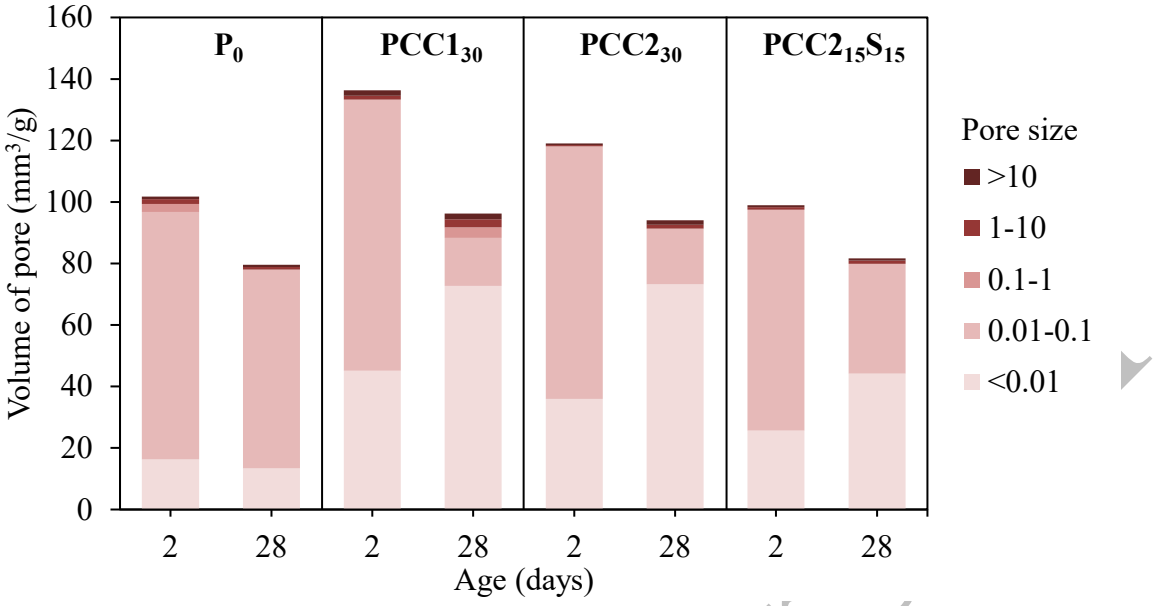

Fig. 5. Pore structure development for the cement pastes between 2 and 28 days (the pore size described is the pore diameter in µm and was limited to 100 µm)

3.2.3 Microstructural analysis

The BSE micrographs of binary and ternary calcined clay systems at 2 and 28 days are shown in Fig. 6, as a means of comparing their microstructures. The main phases were annotated in the last image to indicate the greyscale level of each phase and make the BSE images easier to read. For all mixes, it is clear that the amount of unhydrated particles decreases from 2 to 28 days due to the hydration process.

Figs. 6a and 6b show SEM images of CC1-binary binder respectively at 2 and 28 days, where few visible calcined clay particles are observed (some small darker particles); which suggests its good reactivity, especially at 28 days. No apparent micocrack-type defects are observed, explaining the high compressive strength measured on this paste.

In comparison of $PCC1_{30}$, $PCC2_{30}$ shows smaller amounts of unhydrated cement particles at 2 and 28 days. Knowing that both binary pastes have the same amount of cement, we can conclude that $PCC2_{30}$ has a higher degree of reaction of clinker at both ages. $PCC2_{30}$ has also higher amounts of the dark particles, in addition to some needle-shaped ones, circled respectively in brown and green dashed lines in Fig. 6c, which are probably calcined clay particles, suggesting the lower reactivity of CC2 compared to CC1. In addition, some microcracks pointed in Fig. 6d appear at the edges of these particles, which suggests a poor interface and weakening of the paste by these particles of impure calcined clay.

To precisely assess the nature of the dark and needle-shaped particles, further EDS analyses were carried out at the location of the same marked image (Fig. 6c) in order to obtain the aluminum, calcium, silicon and potassium maps, as depicted respectively in the images of Fig. 7. All these particles show no calcium traces, which confirms they are calcined clay phases. The elemental maps show a strong correlation between Al and K locations, with small amounts of Si, which match with the needle-shaped particles; this indicates that these are muscovite particles. The darkest particles (e.g. the one marked in brown) belong to quartz, given that only Si can be detected in their location using EDS. The existence of these calcined clay impurities prevents cement grains from being uniformly dispersed in the cement matrix, thus causing reduced resistance, yet accompanied by improved porosity, as explained above. Compared to $PCC1_{30}$, CC2-binary binder shows higher amounts of calcined clays impurities (mainly quartz and muscovite) which is consistent with the XRD quantification of both calcined clays. Besides, more portlandite is noticeable in the SEM images of $PCC2_{30}$, which is consistent with TGA results.

Micrographs from the ternary mix (Figs. 6e and 6f) reveal a more heterogeneous cement paste with the presence of both slag and CC2. Slag particles have sharper angles and are less lightly colored than the unhydrated cement grains as annotated in the Fig. 6f. Compared to binary cement pastes, this formulation shows a clear decrease in porosity. Compared to $PCC2_{30}$, the amount of residual unhydrated particles at both ages is greater, but with higher portlandite amount that can be observed on the SEM images and quantified by TGA. This suggests a probable hydration of some slag grains promoted by CC2 filler effect (synergistic effect of both additions). In addition, the different unhydrated cement and slag particles are well distributed in the cement paste, without apparent decohesion or visible cracks, which may explain the paste's good macromechanical property.

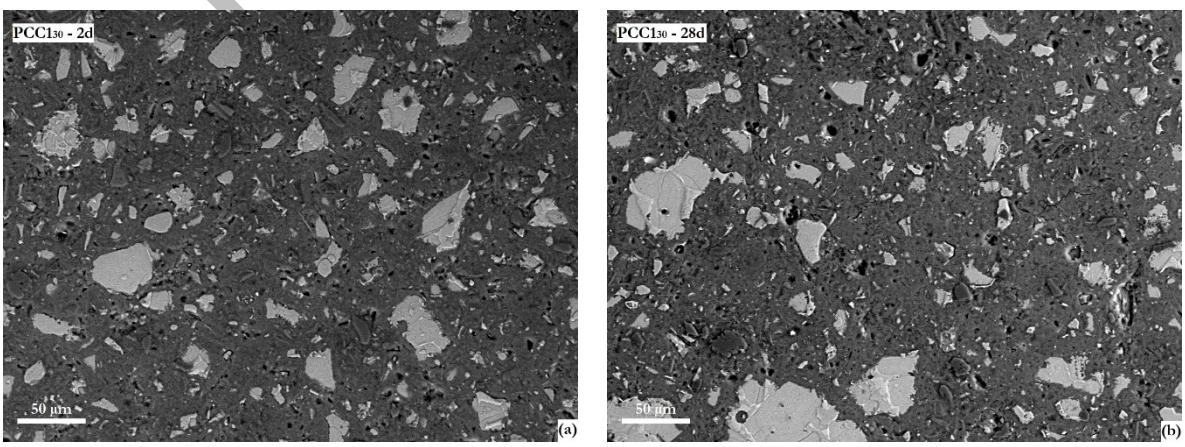

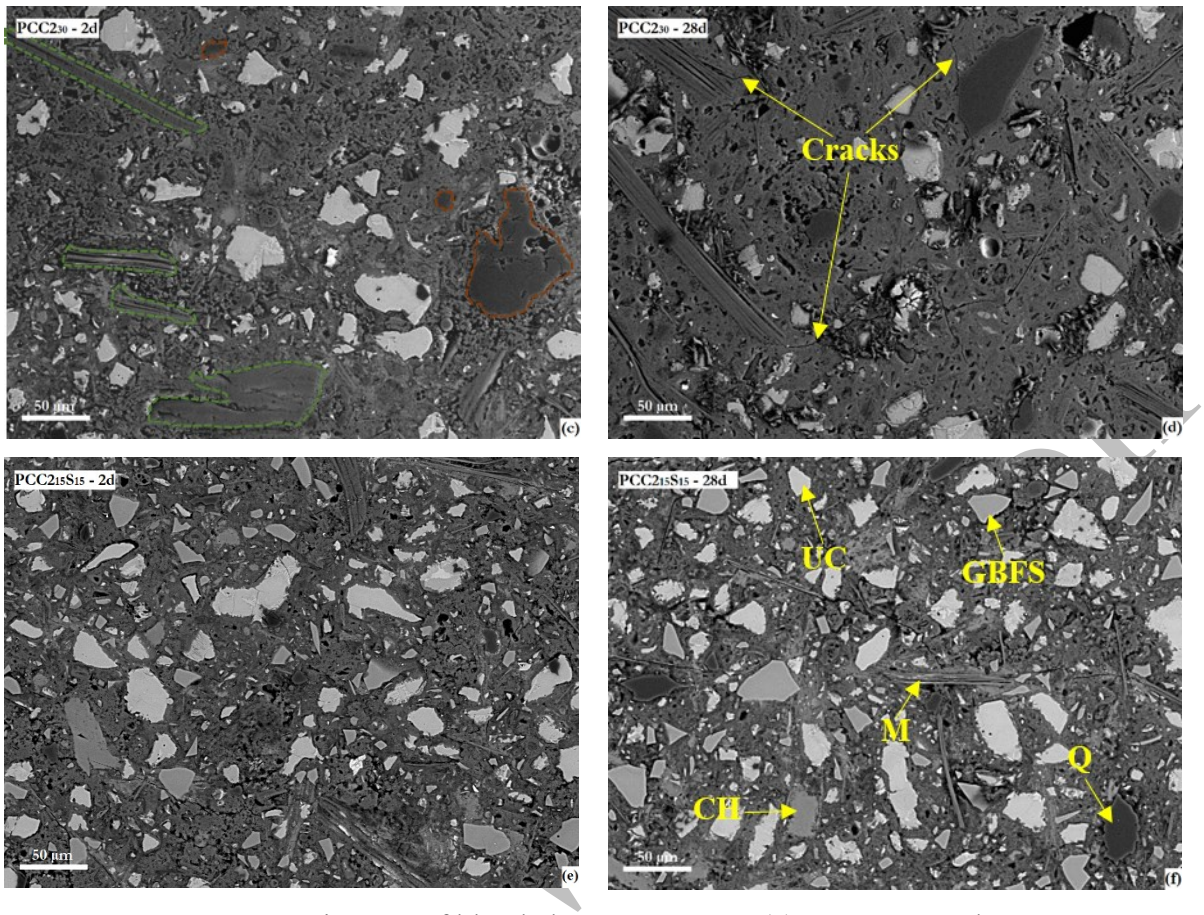

Fig. 6. SEM images of blended cement pastes: (a) $PCC1_{30}$ at 2 days, (b) $PCC1_{30}$ at 28 days, (c) $PCC2_{30}$ at 2 days, (d) $PCC2_{30}$ at 28 days, (e) $PCC2_{15}S_{15}$ at 2 days and (f) $PCC2_{15}S_{15}$ at 28 days. Brown dashed lines show quartz particles, and green ones show muscovite

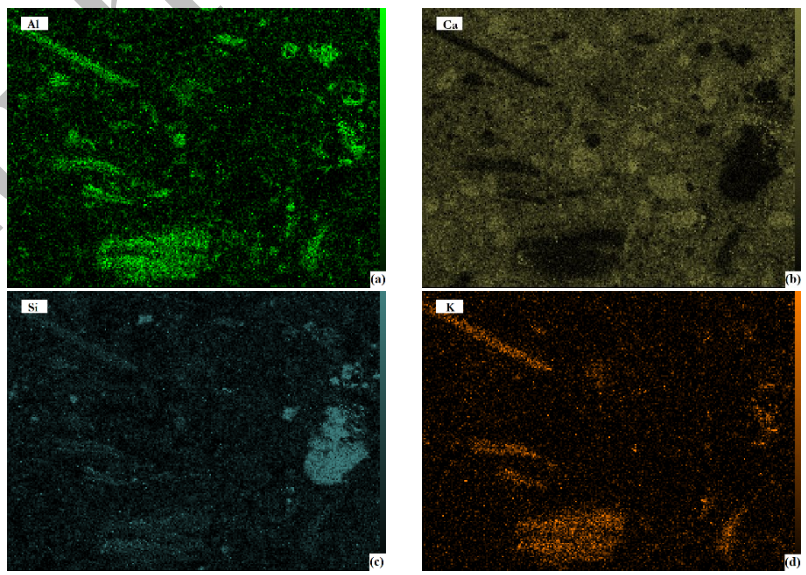

Fig. 7. SEM/EDS elemental maps of $PCC2_{30}$ at 2 days (Fig. 6c) for (a) aluminium, (b) calcium, (c) silicon and (d) potassium

3.2.4 Micromechanical properties of the cement blends

Elastic properties were investigated at the microscale by means of nanoindentation. Figs. 8a-d-g-j show the probability density function in the elastic modulus for the four cement pastes at both 2 and 28 days. Only the elastic moduli less than 60 GPa were depicted for analyzing hydration products' properties. From the outset, a shift can be observed towards higher values of elastic modulus from 2 to 28 days across all mixes since the matrix stiffens with time of hydration. This shift equals 84.6% of the value at 2 days for the ternary binder and is much higher compared to the other cement pastes, reaching 14.3%, 20% and 7.1% respectively for P_0, $PCC1_{30}$ and $PCC2_{30}$. To explain this rate of microstructural development, the results of statistical deconvolution will be further presented and analyzed. The main peaks of hydration products at 2 and 28 days seem higher and narrower in $PCC1_{30}$ which suggests a mono-phase predominance of a hydration product (CSH), and which is consistent with the small amount of portlandite found in $PCC1_{30}$ determined by TGA. The larger distributions in the other cement pastes indicate the presence of multiple hydration products with a higher content of the phase with properties towards the peak.

Likewise, the probability density functions of the hydrates' hardness are shown in Figs. 8b-e-h-k. Unlike elastic modulus, there is a shift towards decreasing hardness from 2 to 28 days in CC2 blended cement pastes (i.e. $PCC2_{30}$ and $PCC2_{15}S_{15}$).

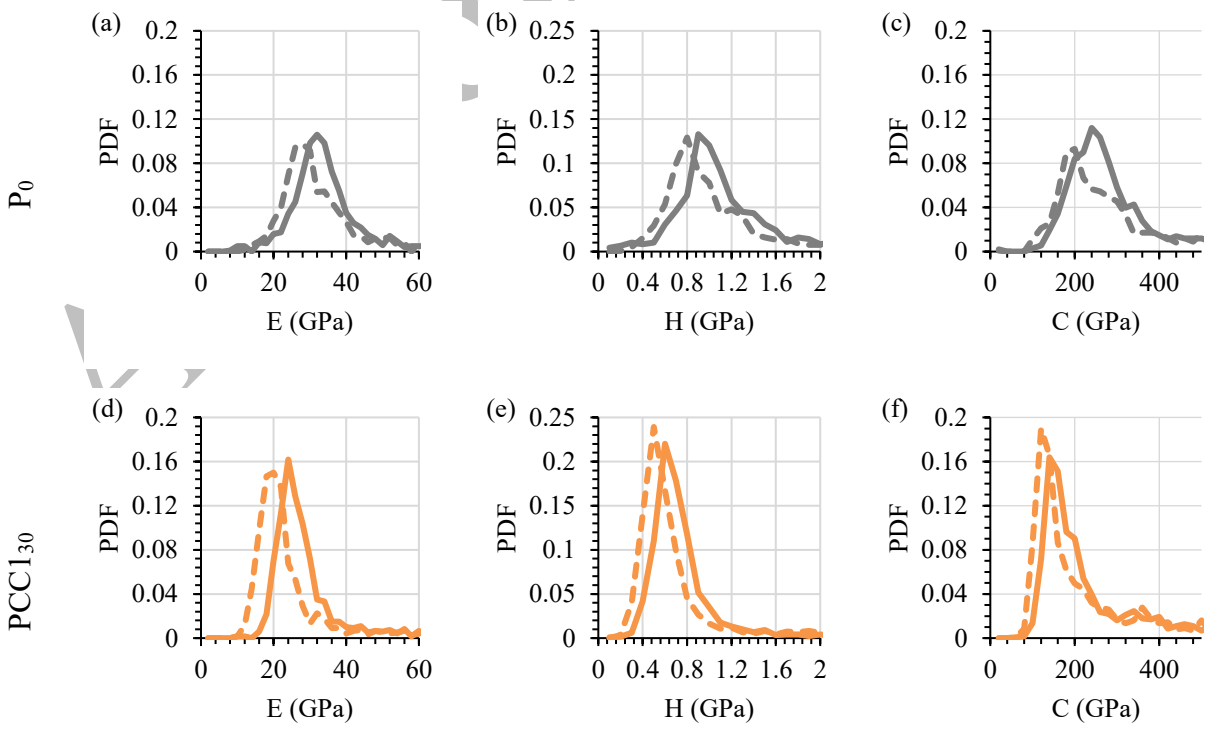

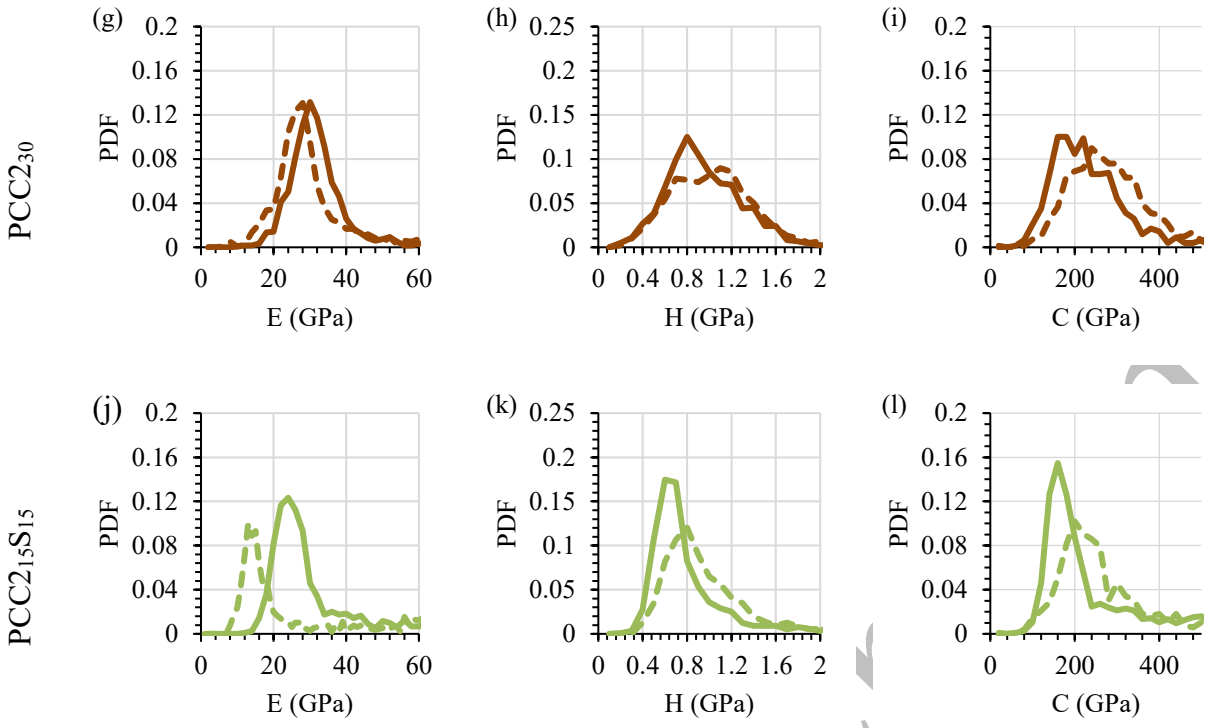

Fig. 8. Probability density functions from statistical nanoindentation of (a-d-g-j) elastic modulus (bin size = 2 GPa), (b-e-h-k) hardness (bin size = 0.1 GPa) and (c-f-i-l) contact creep modulus (bin size = 20 GPa), for the different formulations at 2 and 28 days. Dashed and continuous lines are respectively for 2 and 28 days analysis

Fig. 9 shows the volumetric composition of each cement paste, and the details of deconvolution are summarized in Appendix A (tables A1 and A2 present the micromechanical properties of the clusters issued from statistical deconvolution for 1200 indents probed in the four cement pastes at 2 and 28 days, and Fig A1 allows the visualization of the indents repartition in the two dimensions space composed of elastic modulus and hardness).For P_0, four pure clusters could be detected and attributed as HD CSH, portlandite, interfaces between hydrates and unhydrated particles and finally unhydrated cement grains. The properties from the indents on interfaces can change depending on the amount of different phases in contact with the tip, and thus the standard deviations of these properties are high. Only HD CSH could be detected as the paste's w/b ration is low, and its amount is higher from 2 to 28 days, while it decreases for the unhydrated cement grains as shown in Fig. 9. It is worth noting that CSH can exist in two forms: low-density LD and high-density HD depending on the initial mix proportions of the pastes (mainly water-to-cement ratio, existence of chemical admixtures, mineral additions incorporations). Thus, these two forms have different micromechanical properties, lower for LD CSH, as widely proved in the literature [36].

In the cement blends, this same figure (Fig. 9) shows that the amount of unhydrated cement grains is reduced due to the replacement of Portland cement with mineral additions, and different clusters with more or less pure phases could be detected.

According to Fig. 9, the incorporation of 30% of CC1 resulted in 79% of CSH, higher than the reference mix, with a high amount of LD CSH at 2 days and smaller one for HD CSH. The third cluster was found to belong to both portlandite and interfaces as the amount of portlandite in this paste is low. Then a last cluster that seems to be mainly for unhydrated cement grains but mixed with some quartz particles brought by CC1, due to the slightly decreased mean properties along with higher standard deviation of the properties compared to unhydrated particles properties from P_0. At 28 days, more intermixed phases are detected as clusters, where it seems that there is a higher amount of HD CSH compared to 2 days, probably due to the pozzolanic reaction of CC1.

Besides HD CSH, new clusters appeared in $PCC2_{30}$ at 2 days composed of CC2 most important impurities, namely muscovite and quartz, which could be clearly identified in SEM images of $PCC2_{30}$ shown in Fig. 6. The second cluster was attributed to mixed portlandite and muscovite due to slightly higher mean properties and standard deviation compared to portlandite in P_0. The average properties of the third cluster seem to correspond to only quartz as the standard deviation of the properties is not high, and the fourth one seems to belong to unhydrated cement grains but also to some interfaces because the values of the properties are lower and more dispersed. At 28 days, only three clusters could be detected among which there is HD CSH with higher amount than at 2 days. The higher proportion of CSH observed in both binary binders in comparison with the reference mix is in accordance with the higher fraction of gel pores observed using mercury porosity.

Finally, the ternary binder had clearly a slower reaction at 2 days with still a relatively high amount of unhydrated cement particles (14.3%) and detected unhydrated slag grains. This agrees with the images of $PCC2_{15}S_{15}$ microstructure shown in Figs. 5e and 5f where it visually appears that the paste has higher amounts of unhydrated particles compared to the binary binders. Some portlandite was also found to be mixed with HD CSH. At 28 days, it was hard to differentiate clusters with pure phases due to the high heterogeneity of the cement paste, but it was naturally found to be a mixture of LD and HD CSH, portlandite and unhydrated cement and slag particles.

437

438

439

440

441

442

(a)

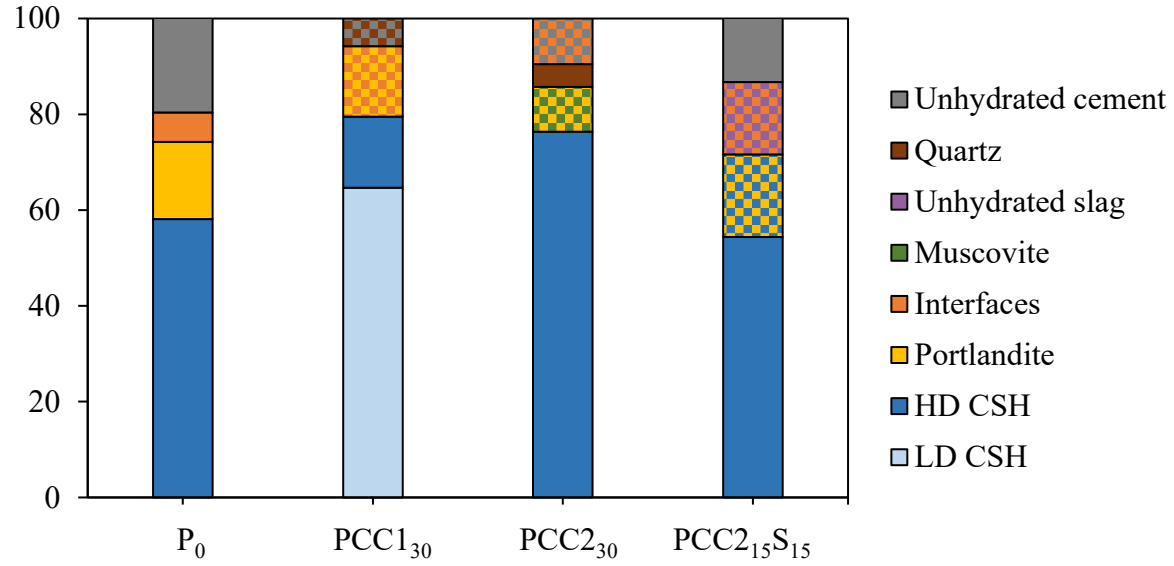

(b)

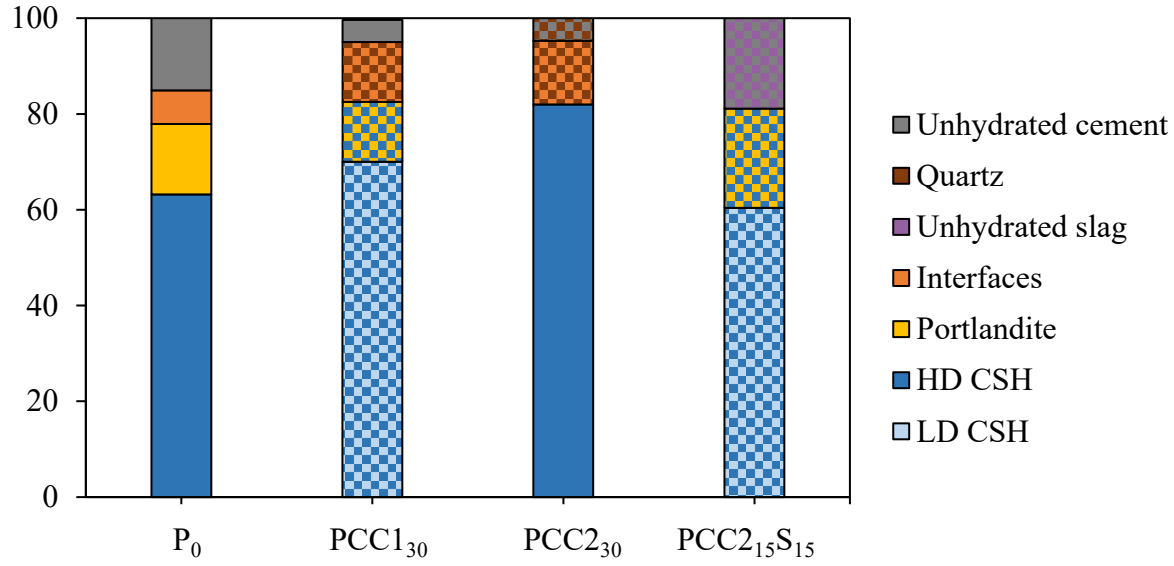

Fig. 9. Cement pastes compositions according to nanoindentation deconvolution results at (a) 2 days and (b) 28 days. Two-tone clusters (with two colours) indicate the existence of two phases in the same cluster according to the legend

In order to understand the cause of low-density phase dominance in $PCC1_{30}$ compared to the other mixes, calorimetric tests were run according to ASTM C1679-08 standard, and the results are depicted in Fig. 10. It can be seen that $PCC1_{30}$ exhibits much higher cumulative heat by gram of cement compared to P_0 after 30 hours of hydration. Based on this observation plus the fact that a higher degree of reaction of clinker was observed by SEM in $PCC2_{30}$, as compared to $PCC1_{30}$, it can be concluded that CC1 is much more reactive than CC2 and moreover that the observed heat difference stems from the CC1 reaction; which is consistent with TGA results and is probably due to its higher amorphous content. Also, a greater amount of cement is hydrated in $PCC2_{30}$, a probable consequence of the filler effect. This suggests that the hydration of calcined clay is the main cause of low-density CSH formation inside the cement paste.

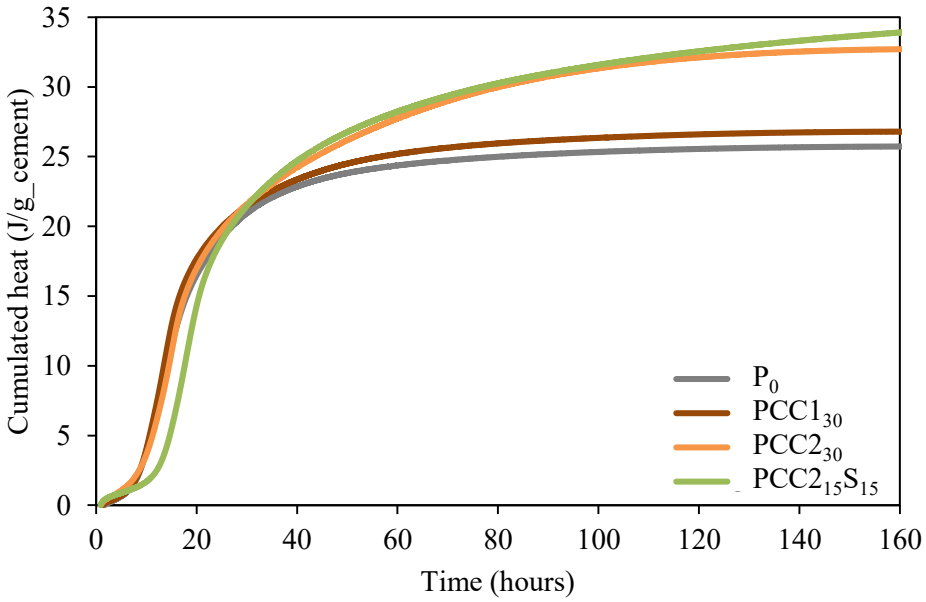

Fig. 10. Normalized cumulative heat (per gram of cement) as obtained by calorimetry

3.2.5 Viscoelastic properties

3.2.5.1 General distribution of creep in the cement pastes

Figs. 8c-f-i-l show the probability density plots of the contact creep modulus for all four mix designs at both early (2 days) and advanced ages (28 days). These plots were limited to 500 GPa so as to compare the hydrates since they account for the predominant creep behavior in cementitious materials. The 2- to 28-day trend changes from one mix design to the next.

For CC2-based pastes, the mean contact creep modulus equals 200 GPa and 240 GPa for $PCC2_{15}S_{15}$ and $PCC2_{30}$ at 2 days, which proves to be respectively equivalent and 20% higher than the reference mix. These mean values are consistent with HD CSH creep moduli according to [49]. Interestingly, these two binders can be used for their strong creep resistance at an early age, with similar or even better properties than CEM I paste albeit a smaller carbon footprint [1,59]. Then, a shift towards a lower contact creep modulus can be observed from 2 to 28 days, which means that these pastes develop good creep resistance at an early age, in decreasing with hydration, a finding that can be explained by the formation of porous hydrates with limited creep properties, which was noticed in mercury porosity results (i.e. the total porosity of these pastes remains relatively unchanged, despite being much finer and containing a larger amount of gel pores).

As for P_0 and $PCC1_{30}$, an increase in the contact creep modulus can be noticed from 2 to 28 days. The contact creep modulus of $PCC1_{30}$ at the peak was 40% and 38.5% lower than P_0 resp. at 2 and 28 days. This indicates a predominance of LD CSH in $PCC1_{30}$, with the formation of some HD CSH at 28 days. These observations are in accordance with calculated proportions of individual phases (shown in Fig. 9) and mercury porosity results, and can be explained by combined calorimetry and SEM results where CC1 was found to be with a high reactivity with lower clinker hydration rate.

3.2.5.2 Creep of individual phases

Fig. 11a shows a portion of indented area (a grid of 5 by 3 indents) in P_0 at 28 days where the imprints of the 2 mN – indents are visible. Two indents from each phase were selected and their load-penetration depth curves and logarithmic penetration depth change with time are shown in Figs. 11b and 11c respectively. The selected indents were boxed in blue, gold and grey to refer to CSH, portlandite and unhydrated cement respectively, identified on the basis of greyscale analysis of the image. It can be noticed visually on the image that the size of imprints in the hydration products is higher than that in unhydrated cement. This difference of size is less visible among indents in CSH and portlandite. This observation is translated in the load-penetration depth curves with smaller maximum penetration depth of indents in unhydrated cement, then in portlandite and CSH.

As for creep properties, it can be noticed that CSH has the highest deformation with a recorded depth change of 31.8 ± 2.6 nm in 60 s creep. Meanwhile, the recorded depth change in portlandite on the two indents is of 20.6 ± 1.0 nm, which represents 65% of that of CSH, commonly considered to be responsible of concrete creep. This means that amount of portlandite in the hydration products and its creep should be taken into account when analyzing the concrete behavior when subjected to creep.

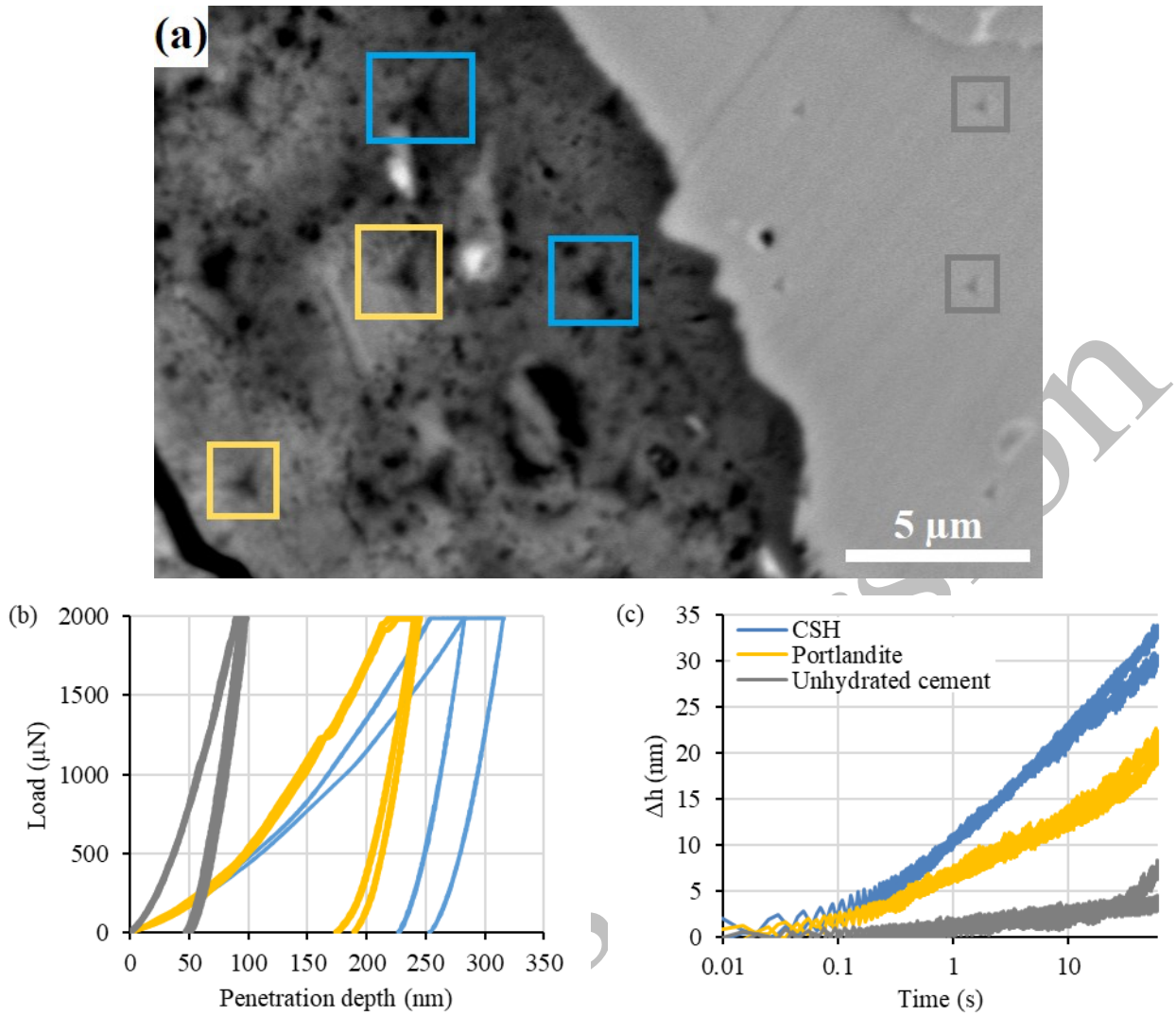

498 **Fig. 11.** (a) SEM image of indented area on P_0 at 28 days. Example of (b) load-penetration depth
499 curves and (c) logarithmic penetration depth change vs. time of CSH, portlandite and unhydrated
500 cement of the boxed indents

501

502 As explained in paragraph 2.2.6, contact creep modulus for CSH phase was calculated for all the
503 mixes at 2 and 28 days. A mean value was taken into account when two types of CSH were found for
504 one mix, and results are shown in Fig. 12. It can be noticed that all the calculated creep properties are
505 within a range of 175 to 266 GPa which corresponds to the values reported in the literature for CSH
506 phases. Some standard deviation values are high; this can be due to existence of some indents of
507 portlandite in CSH-considered cluster, which are of higher contact creep modulus. It can also be
508 noticed that $PCC1_{30}$ creeps more than other formulations at 2 and 28 days, and this is because of the
509 high amount of LD CSH detected in this mix design. As already noticed on the PDFs, the conctact
510 creep modulus tends to decrease in CC2-incorporated pastes, but in general, this property does not

vary signifacantly between 2 and 28 days. This means that the commonly observed trend of increased creep with hydration time is mostly due to the higher fraction of CSH.

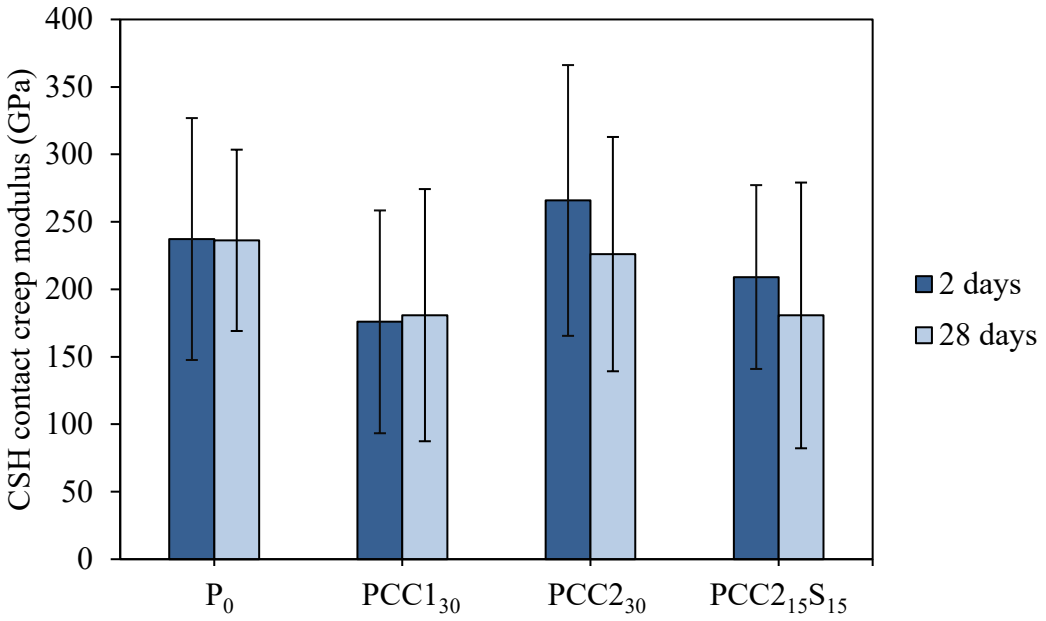

Fig. 12. CSH contact creep modulus for the four formulations at 2 and 28 days

4. Discussion

4.1 Impact of calcined clay composition on the cement paste properties

At the microscale, cement paste can be seen as a heterogeneous material of hard inclusions, which are mainly the unhydrated cement grains, muscovite and quartz contributed by calcined clays and embedded in a porous binding cement matrix constituted of softer hydrated phases, as shown in Fig. 13. Besides promoting the hydration capability of the unhydrated binder, the distribution of hard particles in the hydrate matrix can influence the behavior of cement paste specimens regarding compressive strength. Cementitious materials failure starts with the propagation of microcracks and extends to the formation of major cracks; the existence of tough inclusions in cement pastes results in greater toughness and crack inhibition [60].

At an age of 2 days, the microstructural investigation has shown that $PCC1_{30}$ most important hydration product is LD CSH which resulted in a higher porosity of the blend. Despite its high reactivity at early age proved by combined TGA, SEM and calorimetry, high-grade calcined clay resulted in low-density hydration products, which caused a deterioration of micromechanical properties. However, $PCC1_{30}$ does develop a higher compressive strength than $PCC2_{30}$. This outcome can be explained by the nature of the interface between the hydrate matrix and the hard inclusions: a

smooth transmission of some microcracks to hard particles can prevent their transformation into macrocracks. Indeed, the system of hard inclusions in $PCC1_{30}$ is mainly composed of pure constituents of Portland cement clinker, while $PCC2_{30}$ also contains a sizable amount of quartz and muscovite contributed by CC2, which appear to cause some microcracks on the SEM images. The nature of connection between these two distinct types of hard particles and cement matrices differs, since quartz and muscovite do not participate in the hydration process, while the latter starts from unhydrated cement particles and proceeds as a continuous process over time, which is illustrated in Fig. 13. This finding is consistent with the results presented in [61], wherein the authors observed a high compressive strength even at a 60% replacement rate of natural pozzolan (NP, slowly reactive), which was explained by the optimal distribution of NP and cement grains from an incomplete reaction in the mix.

At 28 days, this same behavior is still observed, although it is slightly reduced at the microstructural scale as the hydration process continues over time. It becomes more effective in $PCC1_{30}$ since CC1 has greater amorphous content, as proven by a higher cumulative heat observed at 7 days, with a stable outlook over the subsequent days of hydration. This explanation is also supported by the SEM images of the microstructure, where it is shown that $PCC1_{30}$ has a uniform distribution of unhydrated cement particles, with no visible microcracks, compared to $PCC2_{30}$, exhibiting fewer cement inclusions and highly distinct quartz and muscovite particles.

The viscoelastic properties of calcined clay-based mixes tend to differ considerably at early age. $PCC1_{30}$ tends to display a LD CSH-predominant microstructure with a small overlapping peak of HD CSH, while $PCC2_{30}$ has a wide distribution that seems to cover the ranges of LD CSH and more of HD CSH. In practice, creep can be both beneficial and harmful depending on the main goal of the material used. A high creep resistance at early age can be beneficial for the prefabrication of large structural elements subjected to their own weight that were unable to gain a sufficient level of resistance. On the other hand, lower creep resistance enables a relaxation of stresses inside the concrete matrix, as caused by temperature variation and shrinkage [62], thus lowering the risk of cracking especially at an early age.

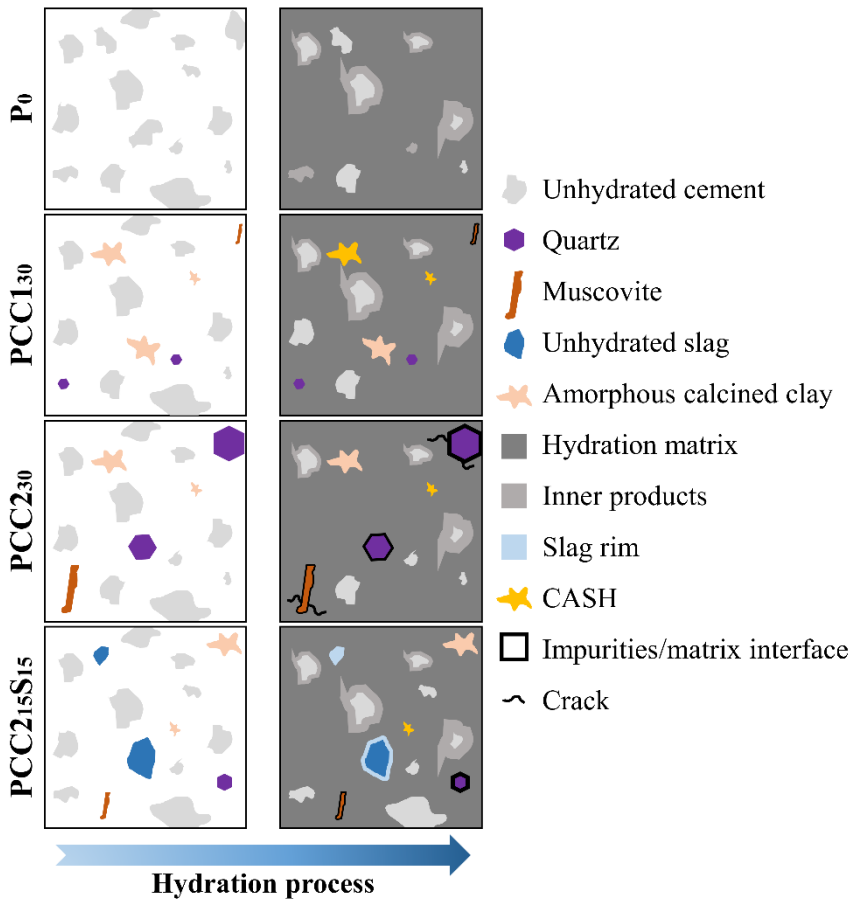

559

560 **Fig. 13.** Schematic representation of the cement pastes microstructures

561

562 *4.2 Synergistic effect of low-grade calcined clay and slag*

563 An interesting synergistic effect between low-grade calcined clay and slag was observed at multiple
564 scales. At the engineering scale, the compressive strength of $PCC2_{15}S_{15}$ is higher, relative to $PCC2_{30}$
565 at early age. At 28 days, the values remained quite similar regarding the overlapping error bars. This
566 result is consistent with those of Khatib and Hibbert [63], or also Li *et al.* [19], who observed an
567 increase in compressive strength with both additions, as compared to a replacement with respectively
568 only slag or only metakaolin. Compared to a replacement with only low-grade calcined clay as
569 measured for $PCC2_{30}$, or with only slag as studied by Gruyaert *et al.* [64], who show lower cumulative
570 heat for a paste with 30% replacement of slag with respect to ordinary Portland cement (w/b=0.5), a
571 higher heat release was shown at 7 days for the ternary binder, compared to both $PCC2_{30}$ and P_0,
572 which tends to be higher at advanced ages, thereby confirming the underlying synergy.

573 At the microscale, a finer pore structure was observed with both additions, as well as a lower total
574 porosity at 2 and 28 days. This finding is in agreement with the results reported in [65], wherein a
575 reduced porosity was noticed for a mix replaced jointly by slag and metakaolin using MIP and

SEM - BSE in ultra-high performance concretes. Also, the ternary binder displayed faster stiffening capability of the mix from 2 to 28 days, with respect to the other mixes.

Conclusion and perspectives

In this study, the utility of low-grade calcined clay in binary and ternary binders was highlighted through a micromechanical study of cement pastes with 30% cement replacement at early (2 days) and advanced (28 days) ages of hydration, supported by microstructural investigation in order to explain macroscopic compressive strength. The main findings of this study can be summarized as follows:

- Binary binder with low-grade calcined clay has 28 days-compressive strength equivalent to ordinary Portland cement paste, results in finer pore structure with equivalent total porosity with respect to ordinary Portland cement paste, all with lower hydration heat compared to high-grade calcined clay
- High-grade calcined clay reacts faster and has higher pozzolanic activity compared to low-grade one
- The fast reaction of high-grade calcined clay results in a higher gel porosity associated with the formation of a low-density phase detected by nanoindentation especially at early age. Therefore, low-grade calcined clay binary cement paste has better micromechanical properties
- The mix proportions do not seem to influence the contact creep modulus of the pastes' CSH
- The calcined clay impurities (mainly quartz and muscovite) prevent good distribution of the unhydrated cement particles and cause some microcracks, which influences the macroscale compressive strength
- Ternary mix with both low-grade calcined clay and slag shows higher 2 days-compressive strength compared to the substitution with only low-grade calcined clay, and has equivalent 28 days-compressive strength to Portland cement mix, with finer pore structure and slightly lower total porosity

These results highlight the interest of mixing low-grade calcined clay with slag to enhance the properties of binary mixes incorporating low-grade calcined clays. Similar performance could be obtained with the same low-grade calcined clay, having a relatively high proportion of crystalline phases, such as quartz, which has a filler effect during hydration, but whose large particles are prone to create weaknesses favoring cracking.

607 Further tests on the nature of interfaces between hard inclusions and the hydrate matrix can be useful
608 in correlating micromechanical observations with the macroscale ones. In addition, classical
609 deconvolution processes should be combined to other techniques to better define clusters of single
610 pure phases.

611 ## Acknowledgements

612 The authors would like to acknowledge the raw materials examinations and tests performed by Vicat.

613

614

615

616

617

618

619

620

621

622

623

624

Appendix A. Deconvolution results

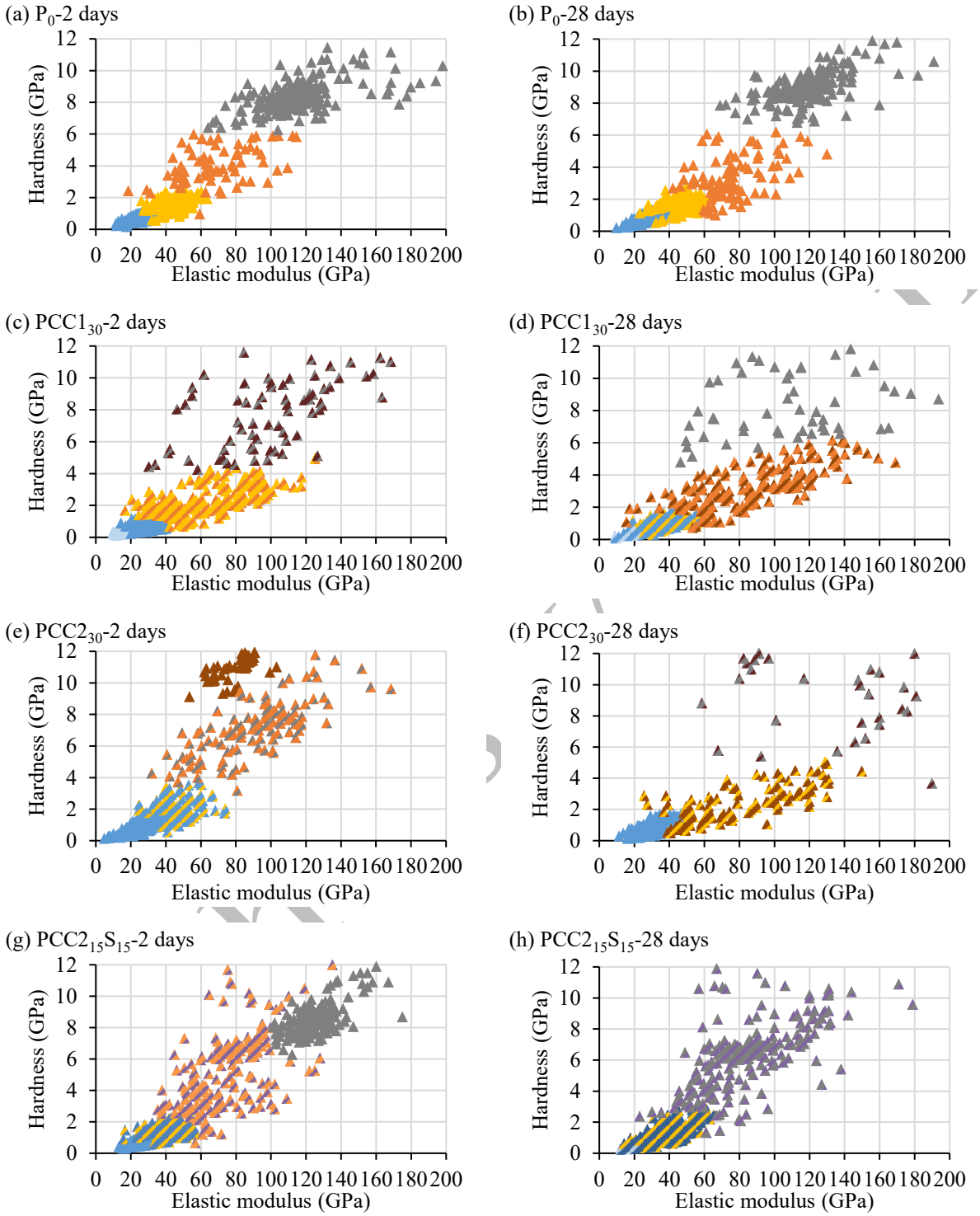

Fig. A1. Results of mechanical clustering using hardness vs. elastic modulus (light blue: LD CSH, dark blue: HD CSH, yellow: portlandite, orange: interfaces, green: muscovite, purple: unhydrated slag, brown: quartz and grey: unhydrated cement)

Table A1

Mean properties ± standard deviation of the clusters resulting from the deconvolution of the four cement pastes and identification of the predominant phase(s) at 2 days.

Paste reference		1	2	3	4
P_0	E (GPa)	26.63 ± 5.17	41.33 ± 7.92	67.69 ± 20.06	117.06 ± 20.86
	H (GPa)	0.79 ± 0.21	1.51 ± 0.38	4.02 ± 1.14	8.44 ± 0.89
	Predominent phase	HD CSH	Portlandite	Interfaces	Unhydrated cement
$PCC1_{30}$	E (GPa)	18.30 ± 3.13	27.72 ± 5.24	64.12 ± 23.14	99.22 ± 31.91
	H (GPa)	0.47 ± 0.12	0.76 ± 0.25	2.38 ± 0.92	7.74 ± 2.09
	Predominent phase	LD CSH	HD CSH	Portlandite + interfaces	Unhydrated cement + Quartz
$PCC2_{30}$	E (GPa)	26.09 ± 5.73	45.72 ± 9.11	79.55 ± 9.84	90.42 ± 26.34
	H (GPa)	0.98 ± 0.34	2.00 ± 0.68	9.84 ± 0.74	7.10 ± 1.78
	Predominent phase	HD CSH	Portlandite + muscovite	Quartz	Unhydrated cement + Interfaces
$PCC2_{15}S_{15}$	E (GPa)	26.44 ± 4.77	37.62 ± 7.28	72.72 ± 17.60	118.50 ± 11.25
	H (GPa)	0.74 ± 0.18	1.33 ± 0.30	4.95 ± 2.11	7.72 ± 0.93
	Predominent phase	HD CSH	HD CSH + Portlandite	Interfaces + Unhydrated slag	Unhydrated cement

642 **Table A2**

643 Mean properties ± standard deviation of the clusters resulting from the deconvolution of the four
644 cement pastes and identification of the predominant phase(s) at 28 days.

Paste reference		1	2	3	4
P_0	E (GPa)	29.73 ± 6.02	41.59 ± 7.39	72.18 ± 16.09	111.63 ± 20.29
	H (GPa)	0.90 ± 0.26	1.54 ± 0.39	2.89 ± 1.08	7.98 ± 1.15
	Predominent phase	HD CSH	Portlandite	Interfaces	Unhydrated cement
$PCC1_{30}$	E (GPa)	23.90 ± 3.72	37.47 ± 7.50	87.77 ± 30.85	109.84 ± 38.88
	H (GPa)	0.60 ± 0.14	0.99 ± 0.32	3.34 ± 1.19	8.14 ± 1.92
	Predominent phase	LD CSH + HD CSH	HD CSH + Portlandite	Interfaces + Quartz	Unhydrated cement
$PCC2_{30}$	E (GPa)	29.50 ± 5.60	78.03 ± 29.82	120.16 ± 40.23	
	H (GPa)	0.88 ± 0.30	2.36 ± 1.11	9.15 ± 2.23	
	Predominent phase	HD CSH	Interfaces + Quartz	Unhydrated particles + Quartz	
$PCC2_{15}S_{15}$	E (GPa)	22.93 ± 3.63	37.85 ± 9.24	82.86 ± 22.81	
	H (GPa)	0.60 ± 0.14	1.36 ± 0.58	6.49 ± 2.50	
	Predominent phase	LD CSH + HD CSH	HD CSH + Portlandite	Interfaces + Quartz + Unhydrated slag and cement	

645

References

[1] K. Scrivener, F. Martirena, S. Bishnoi, S. Maity, Calcined clay limestone cements (LC3), Cement and Concrete Research. 114 (2018) 49–56. https://doi.org/10.1016/j.cemconres.2017.08.017.

[2] M. Murat, Hydration reaction and hardening of calcined clays and related minerals. I. Preliminary investigation on metakaolinite, Cement and Concrete Research. 13 (1983) 259–266. https://doi.org/10.1016/0008-8846(83)90109-6.

[3] G. Puerta-Falla, M. Balonis, G. Le Saout, N. Neithalath, G. Sant, The Influence of Metakaolin on Limestone Reactivity in Cementitious Materials, in: K. Scrivener, A. Favier (Eds.), Calcined Clays for Sustainable Concrete, Springer Netherlands, Dordrecht, 2015: pp. 11–19. https://doi.org/10.1007/978-94-017-9939-3_2.

[4] M. Boháč, M. Palou, R. Novotný, J. Másilko, D. Všianský, T. Staněk, Investigation on early hydration of ternary Portland cement-blast-furnace slag–metakaolin blends, Construction and Building Materials. 64 (2014) 333–341. https://doi.org/10.1016/j.conbuildmat.2014.04.018.

[5] E.-H. Kadri, S. Kenai, K. Ezziane, R. Siddique, G. De Schutter, Influence of metakaolin and silica fume on the heat of hydration and compressive strength development of mortar, Applied Clay Science. 53 (2011) 704–708. https://doi.org/10.1016/j.clay.2011.06.008.

[6] S. Wild, J.M. Khatib, Portlandite consumption in metakaolin cement pastes and mortars, Cement and Concrete Research. 27 (1997) 137–146. https://doi.org/10.1016/S0008-8846(96)00187-1.

[7] F. Curcio, B.A. DeAngelis, S. Pagliolico, Metakaolin as a pozzolanic microfiller for high-performance mortars, Cement and Concrete Research. 28 (1998) 803–809. https://doi.org/10.1016/S0008-8846(98)00045-3.

[8] M.A. Caldarone, K.A. Gruber, R.G. Burg, High Reactivity Metakaolin (HRM): A New Generation Mineral Admixture for High Performance Concrete, CI. 16 (1994) 37–41.

[9] X. Qian, Z. Li, The relationships between stress and strain for high-performance concrete with metakaolin, Cement and Concrete Research. 31 (2001) 1607–1611. https://doi.org/10.1016/S0008-8846(01)00612-3.

[10] J. Ambroise, S. Maximilien, J. Pera, Properties of Metakaolin blended cements, Advanced Cement Based Materials. 1 (1994) 161–168. https://doi.org/10.1016/1065-7355(94)90007-8.

[11] V.N. Dwivedi, N.P. Singh, S.S. Das, N.B. Singh, A new pozzolanic material for cement industry: Bamboo leaf ash, Int. J. Phys. Sci. (n.d.) 6.

[12] B. Sabir, S. Wild, J. Bai, Metakaolin and calcined clays as pozzolans for concrete: a review, Cement and Concrete Composites. 23 (2001) 441–454. https://doi.org/10/dscwv7.

[13] A.H. Asbridge, G.A. Chadbourn, C.L. Page, Effects of metakaolin and the interfacial transition zone on the diffusion of chloride ions through cement mortars, Cement and Concrete Research. 31 (2001) 1567–1572. https://doi.org/10.1016/S0008-8846(01)00598-1.

[14] C. Girodet, M. Chabannet, J.L. Bosc, J. Pera, Influence of the type of cement on the freeze-thaw resistance of the mortar phase of concrete, in: London, 1997: pp. 31–40.

[15] B.B. Sabir, S. Wild, J.M. Khatib, On the Workability and Strength Development of MK Concrete, in: 1996: pp. 651–662.

[16] K. Scrivener, F. Avet, H. Maraghechi, F. Zunino, J. Ston, W. Hanpongpun, A. Favier, Impacting factors and properties of limestone calcined clay cements (LC3), Green Materials. 7 (2019) 3–14. https://doi.org/10.1680/jgrma.18.00029.

[17] A. Zolfagharnasab, A.A. Ramezanianpour, F. Bahman-Zadeh, Investigating the potential of low-grade calcined clays to produce durable LC3 binders against chloride ions attack, Construction and Building Materials. 303 (2021) 124541. https://doi.org/10.1016/j.conbuildmat.2021.124541.

[18] Q.D. Nguyen, T. Kim, A. Castel, Mitigation of alkali-silica reaction by limestone calcined clay cement (LC3), Cement and Concrete Research. 137 (2020) 106176. https://doi.org/10.1016/j.cemconres.2020.106176.

[19] Z. Li, Z. Ding, Property improvement of Portland cement by incorporating with metakaolin and slag, Cement and Concrete Research. 33 (2003) 579–584. https://doi.org/10.1016/S0008-8846(02)01025-6.
[20] F. Cassagnabère, M. Lachemi, M. Mouret, G. Escadeillas, Caractérisation performantielle d'un liant ternaire à base de ciment, laitier et métakaolin, Can. J. Civ. Eng. 38 (2011) 837–848. https://doi.org/10.1139/l11-043.
[21] W. Chen, J. Dang, H. Du, Using low-grade calcined clay to develop low-carbon and lightweight strain-hardening cement composites, Journal of Building Engineering. 58 (2022) 105023. https://doi.org/10.1016/j.jobe.2022.105023.
[22] C.S. Malacarne, M.A. Longhi, M.R.C. Silva, J.P. Gonçalves, E.D. Rodríguez, A.P. Kirchheim, Influence of low-grade materials as clinker substitute on the rheological behavior, hydration and mechanical performance of ternary cements, Case Studies in Construction Materials. 15 (2021) e00776. https://doi.org/10.1016/j.cscm.2021.e00776.
[23] S. Krishnan, D. Gopala Rao, S. Bishnoi, Why Low-Grade Calcined Clays Are the Ideal for the Production of Limestone Calcined Clay Cement (LC3), in: S. Bishnoi (Ed.), Calcined Clays for Sustainable Concrete, Springer, Singapore, 2020: pp. 125–130. https://doi.org/10.1007/978-981-15-2806-4_14.
[24] G. Cardinaud, E. Rozière, O. Martinage, A. Loukili, L. Barnes-Davin, M. Paris, D. Deneele, Calcined clay – Limestone cements: Hydration processes with high and low-grade kaolinite clays, Construction and Building Materials. 277 (2021) 122271. https://doi.org/10.1016/j.conbuildmat.2021.122271.
[25] Y. Chen, C. Romero Rodriguez, Z. Li, B. Chen, O. Çopuroğlu, E. Schlangen, Effect of different grade levels of calcined clays on fresh and hardened properties of ternary-blended cementitious materials for 3D printing, Cement and Concrete Composites. 114 (2020) 103708. https://doi.org/10.1016/j.cemconcomp.2020.103708.
[26] C. Hu, Z. Li, A review on the mechanical properties of cement-based materials measured by nanoindentation, Construction and Building Materials. 90 (2015) 80–90. https://doi.org/10/gd8436.
[27] G. Fang, Q. Wang, M. Zhang, Micromechanical analysis of interfacial transition zone in alkali-activated fly ash-slag concrete, Cement and Concrete Composites. (2021) 103990. https://doi.org/10.1016/j.cemconcomp.2021.103990.
[28] D. Damidot, K. Velez, F. Sorrentino, Characterization of Interstitial Transition Zone (ITZ) of High Performance Cement by Nanoindentation Technique, Proceedings of the 11th International Congress on the Chemistry of Cement,. (2003) 11.
[29] S. Liu, P. Shen, D. Xuan, L. Li, A. Sojobi, B. Zhan, C.S. Poon, A comparison of liquid-solid and gas-solid accelerated carbonation for enhancement of recycled concrete aggregate, Cement and Concrete Composites. 118 (2021) 103988. https://doi.org/10.1016/j.cemconcomp.2021.103988.
[30] B. Hilloulin, M. Lagrange, M. Duvillard, G. Garioud, ε–greedy automated indentation of cementitious materials for phase mechanical properties determination, Cement and Concrete Composites. 129 (2022) 104465. https://doi.org/10.1016/j.cemconcomp.2022.104465.
[31] B. Hilloulin, M. Robira, A. Loukili, Coupling statistical indentation and microscopy to evaluate micromechanical properties of materials: Application to viscoelastic behavior of irradiated mortars, Cement and Concrete Composites. 94 (2018) 153–165. https://doi.org/10/ghdf49.
[32] Z. Luo, W. Li, Y. Gan, K. Mendu, S.P. Shah, Applying grid nanoindentation and maximum likelihood estimation for N-A-S-H gel in geopolymer paste: Investigation and discussion, Cement and Concrete Research. 135 (2020) 106112. https://doi.org/10.1016/j.cemconres.2020.106112.
[33] J. Ying, X. Zhang, Z. Jiang, Y. Huang, On Phase Identification of Hardened Cement Pastes by Combined Nanoindentation and Mercury Intrusion Method, Materials. 14 (2021) 3349. https://doi.org/10.3390/ma14123349.

[34] G. Constantinides, F.-J. Ulm, K. Van Vliet, On the use of nanoindentation for cementitious materials, Mat. Struct. 36 (2003) 191–196. https://doi.org/10/ffkbhj.
[35] G. Constantinides, F.-J. Ulm, The nanogranular nature of C–S–H, Journal of the Mechanics and Physics of Solids. 55 (2007) 64–90. https://doi.org/10.1016/j.jmps.2006.06.003.
[36] M. Vandamme, F.-J. Ulm, P. Fonollosa, Nanogranular packing of C–S–H at substochiometric conditions, Cement and Concrete Research. 40 (2010) 14–26. https://doi.org/10/dgjn5t.
[37] H. Chualin, L. Zongjin, Property investigation of individual phases in cementitious composites containing silica fume and fly ash, Cement and Concrete Composites. 57 (2015) 17–26. https://doi.org/10.1016/j.cemconcomp.2014.11.011.
[38] P. Mondal, S.P. Shah, L.D. Marks, J.J. Gaitero, Comparative Study of the Effects of Microsilica and Nanosilica in Concrete, Transportation Research Record. 2141 (2010) 6–9. https://doi.org/10/cdzcj2.
[39] S. Barbhuiya, P. Chow, S. Memon, Microstructure, hydration and nanomechanical properties of concrete containing metakaolin, Construction and Building Materials. 95 (2015) 696–702. https://doi.org/10.1016/j.conbuildmat.2015.07.101.
[40] C. Hu, Z. Li, Y. Gao, Y. Han, Y. Zhang, Investigation on microstructures of cementitious composites incorporating slag, Advances in Cement Research. 26 (2014) 222–232.
[41] N. Shanahan, A. Markandeya, A. Elnihum, Y.P. Stetsko, A. Zayed, Multi-technique investigation of metakaolin and slag blended portland cement pastes, Applied Clay Science. 132–133 (2016) 449–459. https://doi.org/10.1016/j.clay.2016.07.015.
[42] J. Li, Y. Yao, A study on creep and drying shrinkage of high performance concrete, Cement and Concrete Research. 31 (2001) 1203–1206. https://doi.org/10.1016/S0008-8846(01)00539-7.
[43] L. Charpin, Y. Le Pape, É. Coustabeau, É. Toppani, G. Heinfling, C. Le Bellego, B. Masson, J. Montalvo, A. Courtois, J. Sanahuja, N. Reviron, A 12year EDF study of concrete creep under uniaxial and biaxial loading, Cement and Concrete Research. 103 (2018) 140–159. https://doi.org/10.1016/j.cemconres.2017.10.009.
[44] M. Vandamme, F.-J. Ulm, Nanogranular origin of concrete creep, Proceedings of the National Academy of Sciences. 106 (2009) 10552–10557. https://doi.org/10/dfs8nq.
[45] C. Pichler, R. Lackner, Identification of Logarithmic-Type Creep of Calcium-Silicate-Hydrates by Means of Nanoindentation, Strain. 45 (2009) 17–25. https://doi.org/10/fc8wfn.
[46] M. Vandamme, F.-J. Ulm, Nanoindentation investigation of creep properties of calcium silicate hydrates, Cement and Concrete Research. 52 (2013) 38–52. https://doi.org/10/f5f4zk.
[47] M. Irfan-ul-Hassan, B. Pichler, R. Reihsner, Ch. Hellmich, Elastic and creep properties of young cement paste, as determined from hourly repeated minute-long quasi-static tests, Cement and Concrete Research. 82 (2016) 36–49. https://doi.org/10.1016/j.cemconres.2015.11.007.
[48] Y. Wei, S. Liang, X. Gao, Indentation creep of cementitious materials: Experimental investigation from nano to micro length scales, Construction and Building Materials. 143 (2017) 222–233. https://doi.org/10.1016/j.conbuildmat.2017.03.126.
[49] Y. Li, Y. Liu, Z. Wang, H. Li, J. Mu, Effect of phases on the creep properties of cement paste based on indentation test and homogenization scheme, Construction and Building Materials. 317 (2022) 125957. https://doi.org/10.1016/j.conbuildmat.2021.125957.
[50] Y. Li, Y. Liu, Y. Li, Y. Li, R. Wang, Evaluation of concrete creep properties based on indentation test and multiscale homogenization method, Cement and Concrete Composites. (2021) 104135. https://doi.org/10.1016/j.cemconcomp.2021.104135.
[51] Y. Dhandapani, M. Santhanam, Assessment of pore structure evolution in the limestone calcined clay cementitious system and its implications for performance, Cement and Concrete Composites. 84 (2017) 36–47. https://doi.org/10.1016/j.cemconcomp.2017.08.012.
[52] K. Scrivener, R. Snellings, B. Lothenbach, A practical guide to microstructural analysis, 2015.
[53] B.K. Marsh, R.L. Day, Pozzolanic and cementitious reactions of fly ash in blended cement pastes, Cement and Concrete Research. 18 (1988) 301–310. https://doi.org/10.1016/0008-8846(88)90014-2.

[54] W.C. Oliver, G.M. Pharr, An improved technique for determining hardness and elastic modulus using load and displacement sensing indentation experiments, Journal of Materials Research. 7 (1992) 1564–1583. https://doi.org/10/bdv47f.
[55] G. Constantinides, F.-J. Ulm, The effect of two types of C-S-H on the elasticity of cement-based materials: Results from nanoindentation and micromechanical modeling, Cement and Concrete Research. 34 (2004) 67–80. https://doi.org/10.1016/S0008-8846(03)00230-8.
[56] Z.-H. He, C.-X. Qian, Nanoindentation Characteristics of Cement with Metakaolin Under Different Curing Systems, Nanosci Nanotechnol Lett. 6 (2014) 721–725. https://doi.org/10.1166/nnl.2014.1832.
[57] Y. Liu, A. Liu, S. Liu, Y. Kang, Nano-scale mechanical properties of constituent minerals in shales investigated by combined nanoindentation statistical analyses and SEM-EDS-XRD techniques, International Journal of Rock Mechanics and Mining Sciences. 159 (2022) 105187. https://doi.org/10.1016/j.ijrmms.2022.105187.
[58] M. Frías, J. Cabrera, Pore size distribution and degree of hydration of metakaolin–cement pastes, Cement and Concrete Research. 30 (2000) 561–569. https://doi.org/10.1016/S0008-8846(00)00203-9.
[59] IFPEB, Carbone 4, Brief-Filiere-Beton, France, 2020.
[60] J.H. Brown, C.D. Pomeroy, Fracture toughness of cement paste and mortars, Cement and Concrete Research. 3 (1973) 475–480. https://doi.org/10.1016/0008-8846(73)90085-9.
[61] W. Wilson, J.M. Rivera-Torres, L. Sorelli, A. Durán-Herrera, A. Tagnit-Hamou, The micromechanical signature of high-volume natural pozzolan concrete by combined statistical nanoindentation and SEM-EDS analyses, Cement and Concrete Research. 91 (2017) 1–12. https://doi.org/10.1016/j.cemconres.2016.10.004.
[62] P. Meshgin, K.-K. Choi, M.M. Reda Taha, Experimental and analytical investigations of creep of epoxy adhesive at the concrete–FRP interfaces, International Journal of Adhesion and Adhesives. 29 (2009) 56–66. https://doi.org/10.1016/j.ijadhadh.2008.01.003.
[63] J.M. Khatib, J.J. Hibbert, Selected engineering properties of concrete incorporating slag and metakaolin, Construction and Building Materials. 19 (2005) 460–472. https://doi.org/10.1016/j.conbuildmat.2004.07.017.
[64] E. Gruyaert, N. Robeyst, N. De Belie, Study of the hydration of Portland cement blended with blast-furnace slag by calorimetry and thermogravimetry, J Therm Anal Calorim. 102 (2010) 941–951. https://doi.org/10.1007/s10973-010-0841-6.
[65] P. Zhan, J. Xu, J. Wang, C. Jiang, Multi-scale study on synergistic effect of cement replacement by metakaolin and typical supplementary cementitious materials on properties of ultra-high performance concrete, Construction and Building Materials. 307 (2021) 125082. https://doi.org/10.1016/j.conbuildmat.2021.125082.